2024

Magnetic Sensors: Principles, Methodologies, and Applications

Mohamed Morsy
mohamed.morsy@bue.edu.eg

Magnetic Sensors: Principles, Methodologies, and Applications

Amir Elzwawy, Mahmoud Rasly, Mohamed Morsy, Hasan Piskin, and Marius Volmer

Contents

A. Elzwawy (✉)
Ceramics Department, National Research Center (NRC), Cairo, Egypt
e-mail: aa.elzwawy@nrc.sci.eg

M. Rasly (✉)
Electronic and Magnetic Materials Department, Advanced Materials Institute, Central Metallurgical Research and Development Institute (CMRDI), Cairo, Egypt
e-mail: mrasly@cmrdi.sci.eg

M. Morsy
Building Physics and Environment Institute, Housing & Building National Research Center (HBRC), Cairo, Egypt

H. Piskin
Department of Physics, Boğaziçi University, Istanbul, Turkey
e-mail: hasan.piskin@boun.edu.tr

M. Volmer (✉)
Electrical Engineering and Applied Physics Department, Transilvania University of Brasov, Brasov, Romania
e-mail: volmerm@unitbv.ro

G. A. M. Ali et al. (eds.), *Handbook of Nanosensors*,
https://doi.org/10.1007/978-3-031-16338-8_33-1

Abstract

The necessity for magnetic sensors has evolved rapidly in the recent preceding decades for diverse applications. Various sorts of sensors can directly detect physical properties such as temperature, humidity, and pressure and deliver an output signal associated with the intended parameters. Contrary to these sensors, magnetic sensors monitor the fluctuations in magnetic fields pursued by surrounding objects or events. The magnetic sensors provide data on the direction, rotation, and electrical current and convert them to the corresponding output voltage. Due to the feasibility and wireless response, magnetic field sensors are included in robotics, the automobile industry, magnetic recording, target tracking, human body biomagnetic measurements, and much more. This chapter introduces the background behind the magnetic sensing process and its basics. Afterward, the desired materials for the magnetic sensors are surveyed. The coverage of famous magnetic sensors like the magnetic tunnel junction sensors, giant magnetoresistance sensors, and planar Hall effect sensors is covered. The key parameters for evaluating the performance of the sensor such as exchange bias, sensitivity, and detection limit are highlighted in this chapter. Finally, major industrial and medical applications for magnetic sensors are implemented. This chapter overviews the concepts of magnetic sensors from background to applications and can provide a valuable piece of work for upcoming nanotechnological applications on a wide spectrum.

Keywords

Magnetic field · Magnetic sensors · Exchange bias · Sensitivity · Detection limit

Abbreviations

T_{abs}	Absolute temperature
AMR	Anisotropic magnetoresistance
V_{AMR}	Anisotropic magnetoresistance voltage
AFM	Antiferromagnetic

AI	Artificial intelligence
BP	Barber pole
k_B	Boltzmann's constant
q	Charge of electron
H_K	Crystal anisotropy field
i	Current
CIP	Current in plane
R	Electrical resistance
ECG	Electrocardiography
E_{exchange}	Exchange anisotropy energy
H_{exc}	Exchange anisotropy field
H_{ext}	External magnetic field
FCC	Face centered cubic
FM	Ferromagnetic
$S_{1/f}$	Flicker noise
GMR	Giant magnetoresistance
IC	Integrated circuits
S_{Johnson}	Johnson noise
l	Length
D	Magnetic field detectivity
MNPs	Magnetic nanoparticles
Fe_3O_4	Magnetite
M	Magnetization
θ	Magnetization angle
MCG	Magnetocardiography
E_{Crsytal}	Magnetocrystalline energy
MR	Magnetoresistive
NM	Nonmagnetic
$Ni_{80}Fe_{20}$	Permalloy
PHE	Planar Hall effect
V_{PHE}	Planar Hall effect voltage
PHR	Planar Hall resistance
PET	Polyethylene terephthalate
RKKY	Ruderman–Kittel–Kasuya–Yosida
S	Sensitivity
E_{shape}	Shape anisotropy energy
H_{sh}	Shape anisotropy field
S_{Shot}	Shot noise
SNR	Signal-to-noise ratio
t	Thickness
t_{fm}	Thickness of ferromagnetic material
TMR	Tunneling magnetoresistance
V_{bridge}	Voltage of Wheatstone bridge sensor
w	Width
E_{Zeeman}	Zeeman energy

Introduction

The necessity for apparatus and devices with the ability to sense the Earth and surrounding magnetic fields has been progressively spreading in the last few decades. Various sorts of sensors can provide insights into the medium changes upon their corresponding changes in physical or chemical properties. Sensors are basically identified as a device that provides the possibility of transferring physical phenomena to an electrical response, and thus they might work as a bridge connecting the physical world and the electronic devices world [1]. In other words, they are referred to as the basic part of the chain of measurements that transmits the input parameter to a readable signal convenient for the measurement [2]. Magnetic sensors have supported mankind in investigating and monitoring thousands of functions for numerous eras [3]. Supercomputers and ordinary computers possess raised storage capacities via the usage of magnetic sensors in head drives. Airplanes owe increased safety standards according to contactless magnetic sensing switching. Moving vehicles and automobiles employ magnetic sensors for position tracking and more [3]. Sensing weak magnetic fields can be made using magnetoresistive (MR) sensors microfabricated from single or multilayered magnetic thin films. These sensors are categorized into main sorts of magnetic sensors which are anisotropic magnetoresistance (AMR), tunneling magnetoresistance (TMR), giant magnetoresistance (GMR), as well as the planar Hall effect (PHE) ones.

MR sensors can detect magnetic fields ranging from 10^{-9} T to 10^{-1} T with a linear scale up to ~10^{-2} T, depending on sensor structure and measurement setup. In contrast, the silicon-based Hall effect sensors, developed by a prominent technology and integrated in many applications, are less sensitive, being able to detect magnetic fields larger than 10^{-6} T. Using graphene layers can be patterned flexible Hall effect sensors maintaining a sensitivity of 79 V/(AT) and stable characteristics during bending cycles. A boost in sensitivity up to 1600 V/(AT) but with lower stability in time with deviations of up to 9.3% from one day to another was reported for graphene-based Hall sensors used for magnetic scanning probe microscopy. The MR sensors are microfabricated from magnetic thin films or multilayers consisting of magnetic, antiferromagnetic, and nonmagnetic (NM) thin films using well-defined layers stacking, deposition, and patterning methods. They adhere to the principles of Si-based integrated circuits (IC) technology and are convenient for special applications like integration in microfluidic systems [3, 4]. Not at least, because of the demagnetizing field, most of the MR sensors are sensitive only to in-plane applied fields, and this can be beneficial for magnetic nanoparticle (MNP) detection compared with Hall effect sensors. Thus, each type of sensor brings advantages and drawbacks that must be accounted for for specific applications like magnetometer, rotation sensor, detection of MNPs, etc. Moreover, except for the PHE sensors that possess a native linear response about zero field and deliver a bipolar output signal, the response of MR sensors in magnetic field is unipolar, and a biasing field is required for linearization. However, by using spin valves with crossed anisotropies,

i.e., mutually perpendicular easy axes of magnetization in two neighboring ferromagnetic layers, or by playing with layers dimensions and thicknesses, the output of GMR and TMR sensors can be linearized around zero field.

Magnetic Sensors

Versatile sorts of sensors are employed in every aspect of daily life activities. This comprises humidity sensors [4–6], gas sensors [7], electrochemical sensors [8–11], pressure sensors [12, 13], temperature sensors [14], optical sensors [15–18], and more. Magnetic sensors are defined as a device that can monitor and detect the existence of the magnetic fields and translate this field into an electrical voltage corresponding to the applied magnetic field delivered to the sensing material. Since the magnetic field can easily spread in the free space, it enables a noncontact sensing in a variety of applications, which encompasses neural signal detection, magnetocardiography, autonomous driving, electrical vehicles sensorization, and even opening doors to novel quantum metrology systems. There are several methods to sense the magnetic field mostly relying on the connection between magnetic and electric phenomena [3]. The principle of working for a magnetic field in general depends on the magnetic moment change for magnetic materials when involved in a magnetic field [19]. Numerous physical impacts are demonstrated in the magnetic sensors [20]. The evolution of significantly sensitive and localized magnetic sensors is a propagating area because of the development in the nano- and microfabrication techniques related technologies [21]. However, there is no ideal candidate which fulfills all the needs and requirements for all application areas. This possibility might arise from the discrepancy in magnetic sensors' sensitivity due to the alteration in the sensing element dimensions or the sophisticated working process. In the following, various classifications of magnetic sensors are introduced.

Anisotropic Magnetoresistive Sensors (AMR)

From a broader point of view, AMR can be defined as a generic magnetotransport property that characterizes ferromagnetic metallic substances (as well as their entailed alloys). The AMR outcome was first introduced to the scientific society in 1856 by Lord Kelvin (Willaim T.). Ferromagnetic materials are composed of Co, Ni, Fe, and alloys such as CoFe and NiFe. At the atomic scale, the manifestation of the AMR effect can be clarified as a result of the ferromagnetic metal particular band structure. Indeed, these types of materials are characterized by the state of occupancy of the 3d and 4 s orbitals. The 3d orbitals seem to be partially filled, while the 4 s orbitals seem to be scattered to the *3d* suborbitals in the presence of magnetic fields [22–24]. The electron orbit asymmetry is used mainly to explain the anisotropic magnetoresistance. Consequently, the scattering cross sections of electrons vary where the electrons move parallel or perpendicular to the applied magnetic field.

Because of the asymmetry in electron orbits, spin-orbit coupling arises. Additional significant parameters including longitudinal (ρ_{xx}) and transverse (ρ_{xy}) resistivity depend on the magnetization M values and the accompanying current density J. For polycrystalline conducting magnetic materials (counting ferromagnetic 3d type alloys), the dependence is expressed by subsequent equations [25]:

$$\rho_{xx} = \rho_{\perp} + \left(\rho_{//} - \rho_{\perp}\right) \cos^2\theta \tag{1}$$

$$\rho_{xy} = \frac{1}{2}\left(\rho_{//} - \rho_{\perp}\right) \sin 2\theta \tag{2}$$

where ρ_{xx} is the parallel magnetoresistance and ρ_{xy} is the perpendicular magnetoresistance while θ is the contained angle between current density (J) and magnetization (M) (Fig. 1). The AMR is defined as the disparity of the longitudinal resistivity, while the transverse resistivity variation is termed as the PHE.

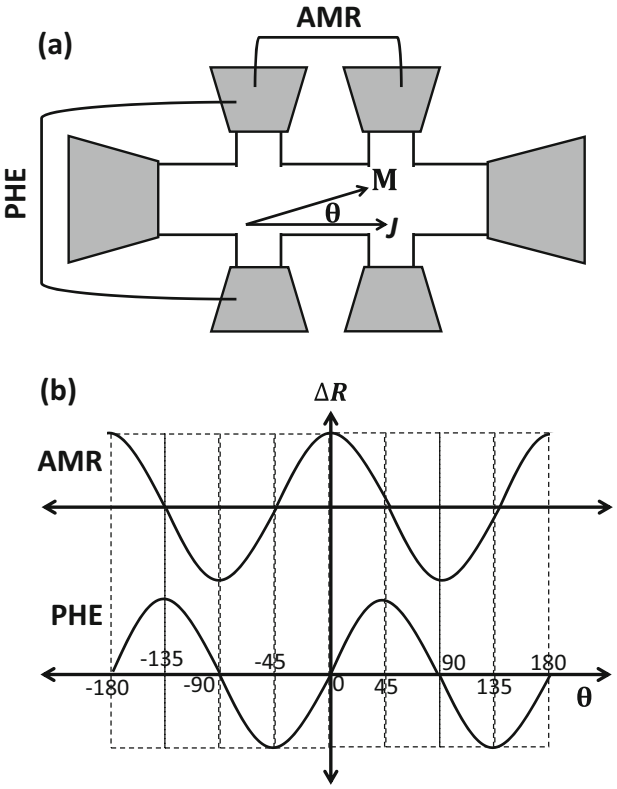

Fig. 1 The AMR and PHE configurations for in-plane and out of plane relativity of magnetization and current density. (Adapted with permission from Ref. [22], (Copyright 2021, IOPSciecne))

Planar Hall Effect Sensors

The signals of the PHE magnetic field sensor depend on the contained angle between magnetic conductor's magnetization and the track of the current flowing through it. The magnetic conductor should be homogeneously magnetized for this application, and in the existence of an applied magnetic field, the magnetization direction should vary predictably, reversibly, and with no-noticeable hysteresis. The magnetic conductor should be uniformly magnetized for this application, and in the company of an externally applied magnetic field, the magnetization direction should vary periodically, reversibly, and with negligible hysteresis.

To achieve this behavior, the layer must be magnetically anisotropic. whenever the above criteria are encountered, the PHE signal designates the magnetization direction that determines the value of the applied perpendicular magnetic field [26–28].

When compared to the AMR, the PHE sensors offer multiple inherent advantages. The largest slope of the AMR sensor as per the θ values (the contained angle among current and magnetization) is achieved at $\frac{\pi}{4} + \frac{n\pi}{2}$, while for the PHE sensor, the largest slope is demonstrated at $\frac{n\pi}{2}$. The PHE offers easy and low-cost fabrication procedures, where the angle θ is equal to the $\frac{n\pi}{2}$ away from the applied magnetic field.

Moreover, the acquired signal from the AMR sensor is usually weak in the range of a few percent and is generally measured over a large DC element connected to a resistance. Hence, temperature variations and aging extremely affect the value of the DC element that is associated with the AMR sensor.

Also, the AMR signal is usually small, at most of the order of a few percent, and it is measured on top of a large DC component associated with the average resistance (see Fig. 1b). Therefore, temperature and aging drifts which affect the DC component are extremely detrimental to AMR sensors. AMR sensors are typically utilized in a Wheatstone bridge configuration of four AMR sensors to generate an output voltage without the DC component. In PHE sensors, such a design is not required as the DC component vanishes at zero.

The AMR signal is also typically small, just a few percent at most, and it is measured on top of a significant DC component related to the average resistance (see Fig. 1b). Thus, AMR sensors are severely harmed by temperature and aging drifts that affect the DC component. To generate an output voltage without the DC component, four AMR sensors are typically used in the Wheatstone bridge configuration. Such a design is not necessary in PHE sensors because the DC component vanishes at zero (see Fig. 1b).

Giant Magnetoresistance Sensors

Magnetoresistance outcome is recognized as an alteration in the electrical resistance of a specific material upon the application of an externally applied magnetic field. Because of the strength and orientation of the magnetic field, the variation in the electrical resistance lies between maximum (R_{max}) and minimum (R_{min}) resistance

magnitudes. The difference in resistance (ΔR) can be normalized with respect to the minimum resistance as a reference value, and thus the magnetoresistance effect can be estimated as follows [22, 29]:

$$MR = \frac{R_{\max} - R_{\min}}{R_{\min}} = \frac{\Delta R}{R_{\min}} \tag{3}$$

The so-called GMR and tunnel magnetoresistance (TMR) influences are the chief two effects incorporated in low-magnetic field sensing applications. GMR was discovered in 1988, when two independent research groups unveiled multilayer structures with tremendous MR values, now known as GMR. These multilayer structures are composed of a stack structure of ferromagnetic layers detached by a tiny layer of nonmagnetic metals. The nominal thickness of each individual layer may reach down to the atomistic scale. One research group headed by Peter Grünberg participated in the first experiments that led to the discovery of GMR where they utilized Fe/Cr/Fe trilayer system [30]. The second research group, directed by Albert Fert, employed a [31], multilayers with the general formula of $(Fe/Cr)_n$ where n might approach 60. For a GMR element, the ferromagnetic layers equal to or more than two layers are insulated by a very slender non-ferromagnetic spacer. The RKKY coupling among contiguous ferromagnetic layers is transformed to antiferromagnetic at specific thicknesses. Consequently, it is preferred for the magnetizations of contiguous layers to orient in antiparallel directions. The device's electrical resistance is often larger in the antiparallel scenario, and the variation might be greater than 10% at ambient temperature as depicted schematically in Fig. 2.

The device's electrical resistance is typically higher with the antiparallel state, and the difference can approach more than 10% at ambient temperature, as illustrated schematically in Fig. 2.

Without the incidence of exterior magnetic fields, antiparallel magnetization is achieved in the ferromagnetic layers. Without the application of the external

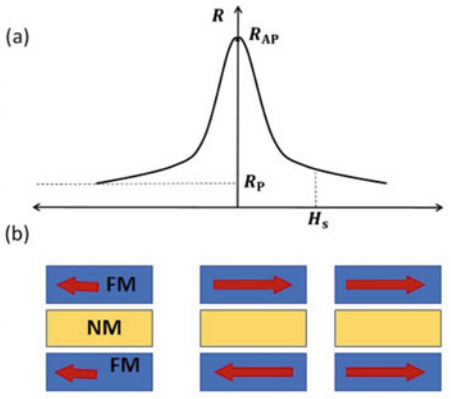

Fig. 2 (**a**, **b**) The configuration of GMR structure, showing the parallel and antiparallel alignments of the magnetization. (Adapted with permission from Ref. [32], Copyright 2016, MDPI)

magnetic field, the ferromagnetic layer magnetizations are aligned antiparallel state. In the presence of an external magnetic field, the magnetic moments are aligned and besides the magnetization is saturated; thereby, the resistance of the multilayers decreases rapidly. The two groups, Grünberg and Fert groups, observed large resistance changes of 6% and 50%, respectively. The amplitude of GMR effect was much smaller for the Grünberg group's system, not because they used a trilayer but mostly because the experiments were carried out at room temperature, whereas the experiments conducted by Fert and co-workers were at very low temperature (4.2 K).

Spin-Valve GMR

This structure consists of two ferromagnetic layers spaced by a small non-ferromagnetic layer but without RKKY interaction. To do this, there must be a huge difference in the coercive fields of each layer to be switched independently. The parallel and antiparallel alignments can be therefore achieved, and the value of resistance would be higher at the antiparallel state [1–3]. The scheme for the spin-valve structure is demonstrated in Fig. 3a.

Pseudo-Spin GMR

The similarities between the pseudo-spin-valve devices and the spin-valve configurations are very close. The major difference is represented in the coercive force of the ferromagnetic layers. The functional magnetic field is varied for the pseudo-spin-valve structure (Fig. 3b) in the first layer, and a weak magnetic field will be applied, while for the other layers, an intensive filed will be used. This, in turn, will flip the magnetization of the first layer before the remaining layers as a result of the applied magnetic field, hence affording the same antiferromagnetic impact that is needed for GMR instruments. The working principle of pseudo-spin-valve devices generally

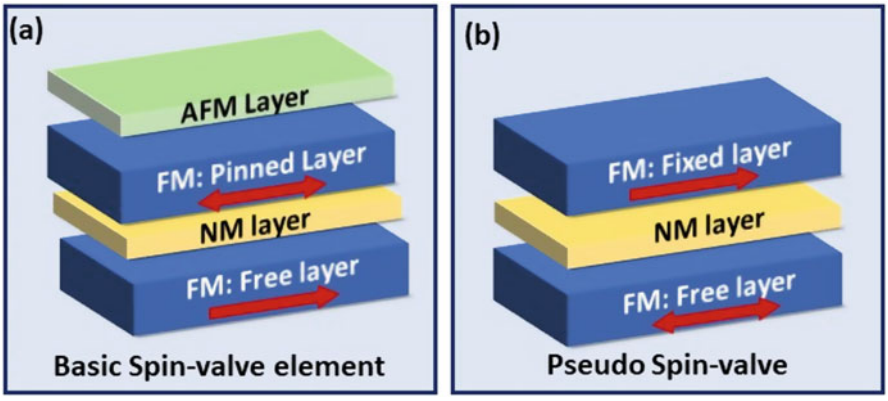

Fig. 3 (**a**) The schematic representation of spin-valve GMR structure (Adapted with permission from Ref. [33], 2013, MDPI) and (**b**) multilayer components of pseudo-spin-valve GMR structure. (Adapted with permission from Ref. [34], Copyright 2008, AIP)

depends on the nominal thickness of the nonmagnetic layer; it must deliver enough thickness to minimize the exchange coupling. The interaction experienced between the two successive ferromagnetic layers must be prevented to grasp complete control over the device.

The GMR discovery achieved a revolution in modern technologies focusing on recent magnetic sensors as well as data storage in hard drives. Currently, the magnetoelectronic phenomena have attracted the attention of many scientists all over the world to investigate their possible applications in many related applications. The discovery of the GMR is a good example for demonstrating the unpredicted scientific findings that may lead to novel technologies with related commercial products.

Tunnel Magnetoresistance

Magnetic tunnel junctions (MTJs) are a famous type of magnetoresistive sensors with numerous layer structures which resemble the spin-valve layer structure. However, a thin insulator layer is introduced here as an insulating barrier, largely aluminum oxide (Al_2O_3) or magnesium oxide (MgO) material. Once the desired voltage has functioned onto the top magnetic electrode, electron spins can tunnel across the insulating barrier to the bottom electrode depending on the magnetization configuration between top and bottom electrodes [54], which might be designated using a spin-dependent tunneling influence [55]. Therefore, the electrons tunneling could be investigated as binary separate spin channels, where Fermi level electrons for the initial ferromagnetic electrode (i.e., FM1) tunnel across the barrier and proceed into free equivalent spin positions at the second ferromagnetic electrode's Fermi level (i.e., FM2). Because of the strong spin imbalance occurring at the Fermi level, ferromagnetic materials behave as spin filters for both cases of up spinning and down spinning electrons of the charge current. Consequently, when there is a parallel magnetization configuration among the upper and lower electrodes, the conduction mechanism arises mainly due to tunneling of the majority electron spin. However, when the magnetization configuration is antiparallel, conduction is due to tunneling of minority electron spin, which restricts the conductance value. Figure 4 is a demonstration of the represented density of states (DOS) and spin-dependent tunneling through a nonconducting barrier.

Since the conductance (G) relies on the entire quantity of the passing electrons through the junction, it can be introduced as the outcome of the Fermi level density of states in both ferromagnetic electrodes as follows:

$$\text{Conductance during parallel configuration} \qquad G_{\mathrm{P}} \propto D_1^{\uparrow} D_2^{\uparrow} + D_1^{\downarrow} D_2^{\downarrow} \tag{4}$$

$$\text{Conductance during antiparallel configuration} \qquad G_{\mathrm{AP}} \propto D_1^{\uparrow} D_2^{\downarrow} + D_1^{\downarrow} D_2^{\uparrow} \tag{5}$$

where $D_{\mathrm{i}}^{\uparrow}$ and $D_{\mathrm{i}}^{\downarrow}$ refers to the density of states volumes in spin up and spin down cases by the Fermi level in the ferromagnetic electrode. Accordingly, when the

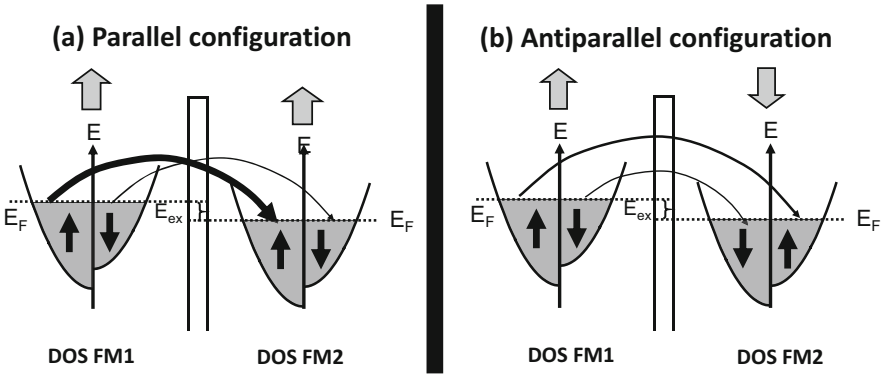

Fig. 4 The represented density of states (DOS) and spin-dependent tunneling through a non-conducting barrier, between ferromagnetic layers having analogous magnetization arrangement (parallel) (**a**) and non-analogous arrangement (antiparallel) (**b**). (Adapted with permission from Ref. [35], Copyright 2020, Elsevier)

magnetization alignments of both ferromagnetic contacts have similar directions, electron-spin tunneling arises among spin bands that have alike density of states, providing a high conductance channel. Conversely, when the magnetization alignments are antiparallel, electron-spin tunneling arises among spin bands that owe changed density of states delivering a reduced conductance channel. Therefore, as the conductance has an inverse proportion to the electrical resistance ($R = 1/G$), the TMR ratio might be stated as the alteration in resistance among the parallel and antiparallel magnetization arrangements as follows [36, 37]:

$$TMR, \% = \frac{R_{AP} - R_P}{R_P} \times 100 = \frac{G_P - G_{AP}}{G_{AP}} \times 100 \tag{6}$$

Because of the oxide insulator, MTJs demonstrate a great resistance difference between parallel and antiparallel states and thereby a higher MR ratio than in the case of spin-valves sensors.

During the foremost age of MTJs with Al_2O_3 layer as an amorphous barrier, TMR ratio was in the range of 70% [56]. Thereafter, presenting MgO as a crystalline barrier led to the enhancement of TMR ratio reaching 200% that exists in Fe/MgO/Fe junctions at ambient temperature [57].

MTJ Layer Structures

Basic Layer Structures

The standard structure of a MTJ layer structure comprises dual ferromagnetic layers detached by a nonconducting nonmetallic thin barrier; herein first ferromagnetic layer possesses a fixed magnetization direction (*known as reference layer*), and the second is free to rotate (referred to as *free or sensing layer*) with the variation in the applied magnetic field. The reference layer magnetization can be pinned through a

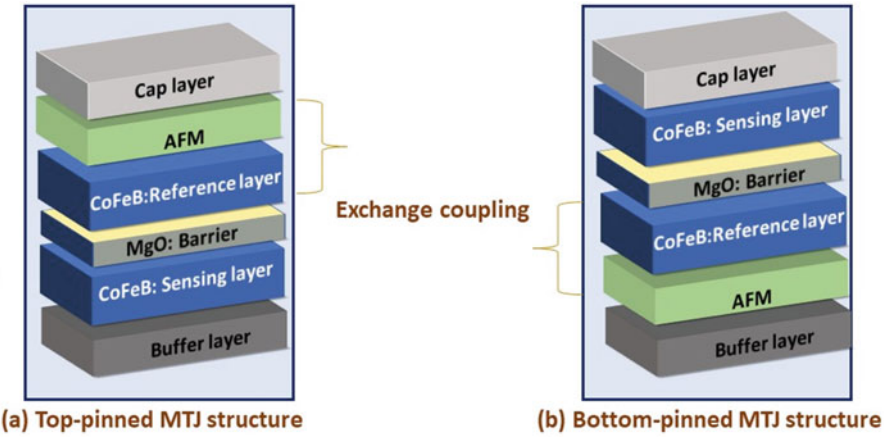

Fig. 5 The representation of MTJ structure. (Adapted with permission from Ref. [37], Copyright 2015, MDPI, and from Ref. [38], Copyright 2016, Springer)

specific direction by the occurring coupling with a thick antiferromagnetic (AF) material layer as IrMn. The AF layer generates an exchange-bias result, which pins the magnetization of the adjacent ferromagnetic layer through a certain direction by annealing under an external magnetic field. As shown in Fig. 5, when an AF layer is coupled with the top (bottom) ferromagnetic layer, the structure is then called a top (bottom) pinned MTJ. Overall, the layer structure can't be deposited directly on top of a substrate because of a roughness issue. Therefore, seed layers or buffer layers must be sputtered first to enhance the surface interface, enhancing the tunneling probabilities across layer structures and principally insulator barriers. Finally, to hinder the corrosion and oxidation of the layer structure from the surrounding medium, a thin capping layer is frequently deposited on the top of the structure.

The Synthetic Ferromagnetic Structure

With SF structure, magnetization alignments can be installed. This structure ensures an antiferromagnetic coupling between the two ferromagnetic contacts (FM1 and FM2) via the interlayer-exchange coupling effect, i.e., across a nonmagnetic barrier (NM). Since the ferromagnetic layers are free to rotate, e.g., no exchange bias, a low effective magnetic thickness t_{eff} can be adapted, and an increased physical free-layer thickness can be preserved according to the following: $t_{\text{real}} = t_{\text{FM1}} + t_{\text{NM}} + t_{\text{FM2}}$.

$$t_{\text{eff}} = \frac{M_1 t_1 - M_2 t_2}{M_{\text{eff}}} \tag{7}$$

where t_{i} and M_{i} are the thickness and magnetization, correspondingly, of both FM layers $i = 1, 2$, and $M_{\text{eff}} (= M_1 + M_2)$ is the SF free-layer effective magnetization. The effective magnetic moment and thickness can be therefore specified by minimizing

the self-demagnetization field formed using the free layer. Nevertheless, a lesser effective magnetic thickness generates an offset field H_0 due to enhancement in the Neel interlayer coupling field, viewing $1/t_{\text{eff}}$ dependence. Thus, an adaptation of synthetic antiferromagnetic coupling across the nonmagnetic spacer is more appropriate for applications.

The Synthetic Antiferromagnetic (SAF) Structure

Synthetic antiferromagnetic (SAF) coupling structure has announced to enhance the exchange-bias field, i.e., improve magnetic stability, and to decrease the occurring magnetostatic coupling among the free and the reference layer owing to a minor resultant moment for the SAF structure. The SAF includes a layered structure, whereas both ferromagnetic layers are imparted by a low thickness nonmagnetic layer (NM). One ferromagnetic layer (FM1) is in contact with an antiferromagnet layer through the exchange coupling effect, while the remaining ferromagnetic layer (FM2) is coupled antiferromagnetically to the FM1 through (Ruderman–Kittel–Kasuya–Yosida) RKKY interaction [66]. This contacting interaction displays the coupling impact through two ferromagnetic layers parted by a separating nonmagnetic spacer and fluctuates between antiferromagnetic and ferromagnetic layers based on the thickness of the nonmagnetic spacing layer.

Sensor Materials

Polycrystalline Sensing Layers

To ensure low-noise characteristics of MTJ sensors, the origin of the frequency-dependent (1/f) noise and thermal noise should be identified and minimized. For that, the later has admitted to the reduction of junction resistance and the former is by improving the quality of the layer structures. According to the application and the limit of detection, magnetic sensors can be categorized. For extremely low-sensing applications such as magnetocardiography, MTJs are the most promising magnetic sensors. Therefore, the requirements and recent advances on magnetic materials in MTJ structures are discussed.

Figure 6 shows a schematic structure of the MTJ sensor processed with the soft-pinning technique. Soft-pinning technique is applied to obtain a cross-magnetization between reference and sensing layers. Cross-magnetization is mandatory to induce a kind of coherent rotation of sensing layer magnetization with the change in external magnetic field, i.e., linear transfer from parallel state to antiparallel state and vice versa. In the forthcoming section, the linearization techniques will be discussed in more detail. In most cases, soft-magnetic materials such as permalloy (NiFe) are strong candidates as sensing magnetic materials because it has small magnetic anisotropy, which defines the special resolution of magnetic sensors. Therefore, NiFe is introduced as a sensing layer. However, it has fcc 111 texture, and CoFeB (CFB) must acquire bcc 100 texture in order to improve electron-spin tunneling and thereby high TMR ratios. To reduce the propagation of fcc texture from NiFe over

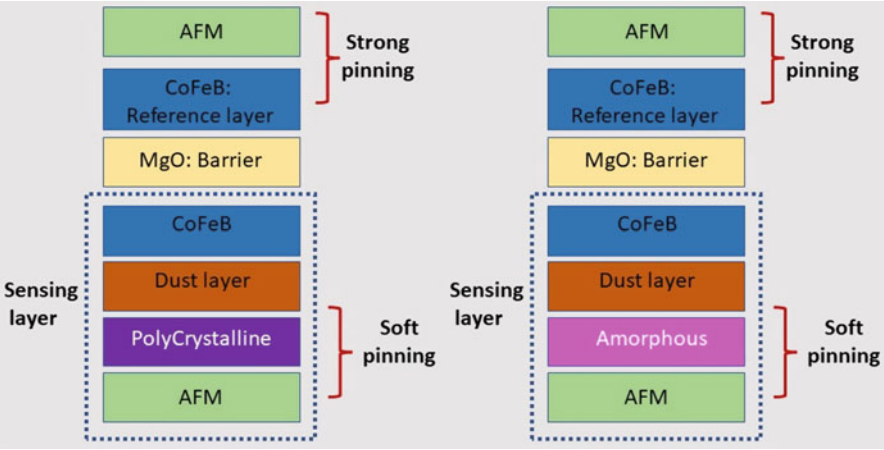

Fig. 6 Magnetic tunnel junction element with polycrystalline sensing layer (left) (Adapted with permission form Ref. [37], Copyright 2015, MDPI) and magnetic tunnel junction element with amorphous sensing layer (right). (Adapted with permission from Ref. [39], Copyright 2023, AIP)

the layer structure, a thin dust layer of Ta, Ru, or W has to be grown on top of NiFe. However, the difference in the crystal orientations has still influenced the texture of CoFeB, enriching the source of noise within the layer structure and thereby reducing TMR ratios. Also, the soft-magnetic properties of NiFe degrade by annealing at high annealing temperature ($\geq$ 350 °C), which is required to achieve a high TMR ratio.

Amorphous Sensing Layers

Alternatively, amorphous soft-magnetic alloys like CoFeBX, where X is Si, Ta, and Hf, are needed owing to their high crystallization temperatures [40] (Fig. 6). Particularly, introducing Ta to CoFeB leads to increasing the crystallization temperature to more than 500 °C. There is no (crystalline) template transferring from the sensing layer to the spacer, which promotes in high tunneling magnetoresistance ratio (TMR).

Linearization Techniques

The transfer curve can be considered as an indicator for the magnetic sensor performance where the resistance depends on the applied field. A typical magnetic tunnel junction with parallel/antiparallel magnetization configuration cannot be used as a magnetic sensor. This is because the transfer curve exhibits an abrupt change in the resistance values while the magnetization configuration changes between parallel/antiparallel states, generating a squared hysteresis loop as shown in (Fig. 7a).

In order to use MTJ as a type of magnetic sensors, the transfer curve must show linearity without a hysteresis curve throughout the active operating range. This happens only if there is an orthogonal-magnetization configuration between the sensing and reference layers (Fig. 7b). Several techniques have been reported through the literature to produce linear transfer curves. Figure 8 summarizes the essence of the most usable techniques.

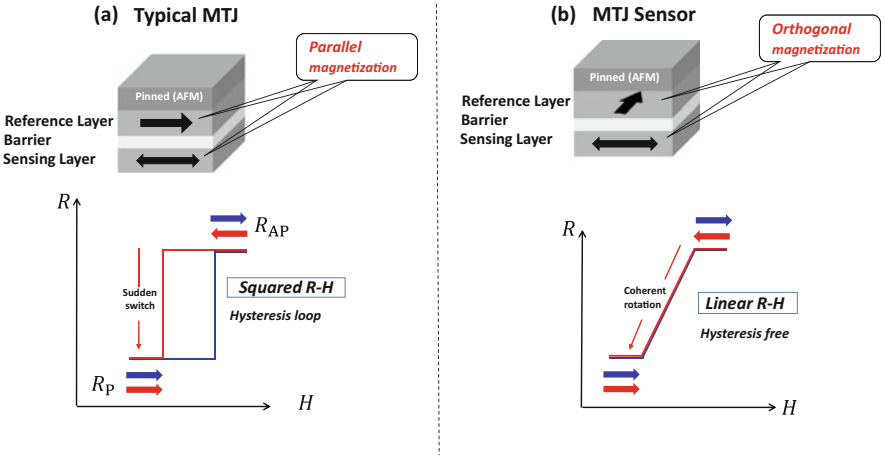

Fig. 7 The change in resistance with magnetic field showing square and linear transfer curves. (Adapted with permission from Ref. [37], Copyright 2015, MDPI)

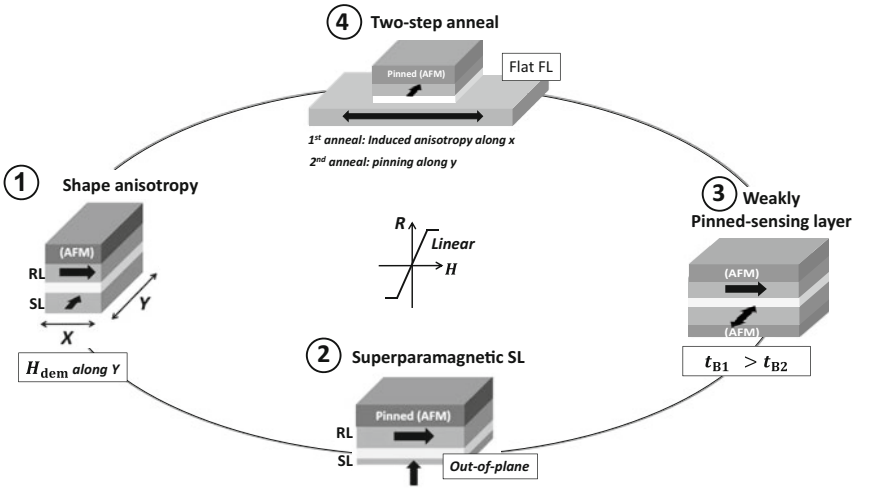

Fig. 8 MTJ sensor linearization techniques. Orthogonal-magnetization configuration between the sensing and reference layers (Fig. 7b)

Shape Anisotropy Technique

In addition to magnetocrystalline anisotropy, the shape anisotropy effect of the ferromagnetic material can control the magnetoresistance effect in magnetic tunnel junctions and the linearity of the transfer curve as well [46]. Lu et al. [46] investigated the shape of the transfer curve in two different MTJ series. In the first series, they have patterned MTJs with the same nominal areas and different shapes; the morphology of the rectangle demonstrated a needlelike rectangle normal to the easy-axis of the film to a squarish profile in the intermediate of the series to a thin needle at the right end. In the second series, they have patterned junctions with the same shape but different sizes, all rectangle junctions having a 5:1 aspect ratio through the easy-axis direction. The study showed that shape anisotropy has more importance than intrinsic magnetocrystalline anisotropy for the linearization process. One can easily generate a linear transfer curve using needlelike rectangular junctions, in which the shape anisotropy dominates the magnetization direction perpendicularly to the thin film easy-axis.

Superparamagnetic Sensing Layer

A different technique uses a thin layer of CoFeB as a superparamagnetic sensing layer. This thin layer can be utilized to attain a response with linearity and non-remarkable hysteresis, along with unpretentious designs and without the necessity of the shape anisotropy effect. Since the magnetization of the CoFeB turns to be an out-of-plane direction at thicknesses less than 1.5 nm, an orthogonal-magnetization configuration will be presented with the already-existing in-plane magnetization of the reference layer. A linear response with change in external in-plane magnetic field can be attained.

Soft-Pinned Sensing Layer

Magnetic tunnel junction (MTJ) stacks that have a softly pinned sensing layer are composed of multilayer structure having a dual antiferromagnetic film, with one layer located close to the pinned layer while the second layer is adjacent to the sensing layer. Thus, together, antiferromagnetic layers manipulate the ferromagnetic layer magnetization in an orthogonal direction to each other by manipulating the exchange-bias directions. To do this, the exchange-bias field (H_{ex}) of the sensing layer (FM2) should be smaller than the exchange field regarding the reference layer (FM1), enabling high sensitivity linear response. This is because the field at saturation is defined typically by the sensing layer's exchange coupling magnitude.

A suitable selection of the antiferromagnet thickness can determine the desired difference in the blocking temperature and thereby the exchange-bias effect. As exemplified in Fig. 9, the blocking temperature (T_{B2}) of the adjacent antiferromagnetic layer to sensing layer has to be lower than the blocking temperature (T_{B1}) of the

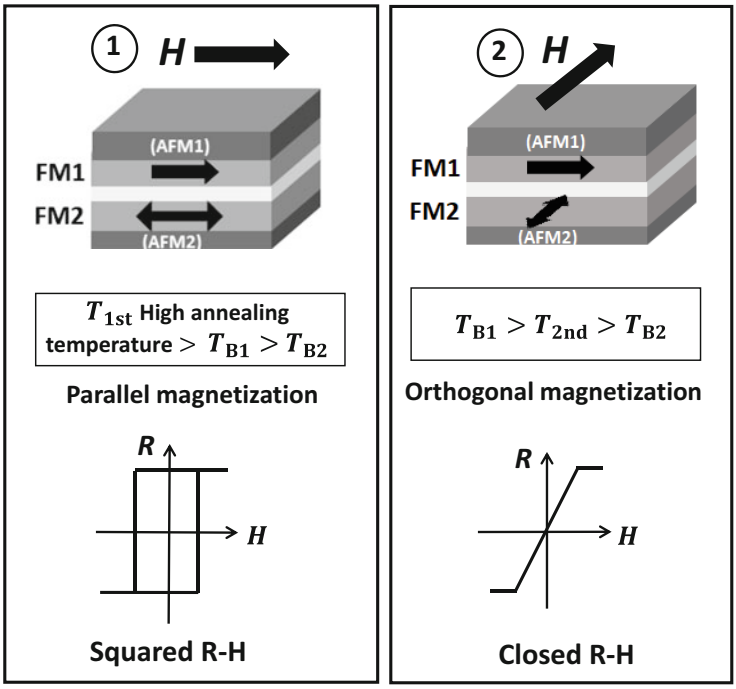

Fig. 9 MTJ with soft-pinning free layer (FM2/AFM2). The annealing temperature during the first step T_{1st} is greater than blocking temperatures of AFM1 and AFM2, and then the exchange-bias directions of the top pinning (AFM1/FM1) and bottom pinning (FM2/AFM2) will be directed through the external magnetic field, showing a squared R-H change. During the second step, annealing temperature T_{2nd} is greater than the blocking temperature of AFM2 only; therefore, the direction of exchange bias at the bottom pinning (FM2/AFM2) will be rotated along applied field direction. (Copyright 2018, MDPI publisher, and Ref. [47])

adjacent antiferromagnetic layer to reference layer. The cross-magnetization configuration can be therefore adjusted through two consecutive annealing steps under application of magnetic field. In the first step, the annealing temperature ($T_{1st} > T_{B1} > T_{B2}$) is high enough to crystallize the layer structure and set the direction of magnetizations though a certain direction. In the second step, the annealing temperature (T_{2nd}) is only higher than T_{B2} to reset the direction of magnetization of sensing layer along an orthogonal direction.

Blocking temperature (T_B) is the temperature at which the exchange-bias field disappears, closely reaching the Neel temperature (T_N) for raised thickness antiferromagnetic films having an increased grain size, whereas for thin films $T_B << T_N$ because of finite size influences. Consequently, as the T_b is tremendously dependent on the AFM material as well as its thickness, therefore, for bottom pinned layers, a specific temperature stability is needed. The same or different AFM materials can be employed to achieve the sensing layer blocking temperature, utilizing its thickness to verify that T_{B1} (reference layer) > T_{B2} (sensing layer). Consequently, two successive

annealing stages through an orthogonal in-plane applied magnetic field at dissimilar temperatures, the crossed formation among the magnetization of the sensing, and the pinned layers can be defined properly. The initial annealing step, executed at an increased temperature $T_{1st} > T_{B1} > T_{B2}$, assigns both reference and sensing layer magnetizations in the identical orientation, whereas the subsequent annealing stage is conducted at a lesser temperature $T_{B1} > T_{2nd} > T_{B2}$ which orients the magnetization of the softly pinned sensing layer with a normal configuration to the lower one.

Two-Step Annealing Technique

In this technique, researchers set the orthogonal-magnetization configuration by applying two-consecutive annealing steps, in which orthogonal annealing magnetic fields should be adapted at different annealing temperatures. The easy-axis of magnetization of the sensing layer is set first by the first annealing step. For that, top-pinned MTJs are very suitable multilayer structures, such that the sensing layer must be completely free from the demagnetization effect, e.g., not patterned as shown in Fig. 10. Thereafter, a second annealing step is needed to set the pinning direction orthogonal to the sensing layer magnetization.

Sensor Design

The magnetic sensor design relies on multiple criteria that must be taken into consideration in order to have a functional device for different applications. Sensor design and structure depend to a large extent on the type of application. The overall performance of the magnetic sensor will be affected by the constituents of its parts. For example, the structure of the sensing layer in addition to the sensor's packaging can affect the linearity and thermal behavior of the sensor. These parameters have a direct effect on the sensor's performance; hence, precise knowledge must be acquired before starting the improvement of the sensor. Hereinafter, the bridge and in array structure of TMR will be discussed.

Array Sensor

The background noise level is a serious implication when using MTJ sensors in numerous applications because of their voltage bias dependence and reduced electrical robustness. A proposed approach to decrease the influence of the voltage bias requirement is to employ an array of serially connected MTJ sensors as shown in Fig. 11. Under such a configuration, the effect of the high bias voltage would be reduced across each junction, maintaining a high TMR ratio. However, the main disadvantages of array sensors are the broadening in linear transfer curve (low spatial resolution), and also they possess a higher noise level in comparison with noise of a single MTJ sensor.

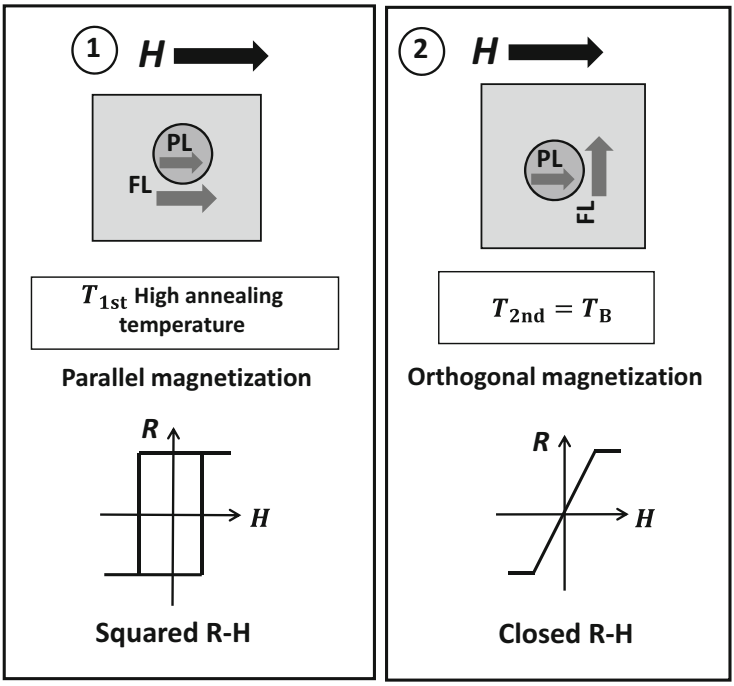

Fig. 10 MTJ with un-patterned (flat) free layer. The first annealing step will result in parallel magnetization, where the induced magnetocrystalline anisotropy of the free layer (FL) in the bottom electrode will be parallel to the pinning direction of the pinned layer (PL). Thereafter, the sample will be rotated by 90^0 and then reannealed at a temperature equal to blocking temperature of AFM. This results in an orthogonal-magnetization configuration between free and pinned layers. (Adapted with permission from Ref. [47], Copyright 2018, MDPI, and Ref. [45], Copyright 2021, IOP science)

Among all, these sensors are sometimes utilized in severe environments, where temperature drifts may affect the output voltage (V_{out}). Like any other resistive sensor, the electrical resistance of MTJs and spin-valves commonly changes as the temperature changes. Thus, any fluctuations in the output voltage that originated from temperature drift must be differentiated from those originated from the sensing magnetic field. One possible solution for these issues is to integrate sensors into Wheatstone bridge architecture as shown in Fig. 12.

Bridge Sensor

Wheatstone bridges are a specific type of electrical circuit used mainly to measure the value of unknown resistance and are composed of four resistances. The TMR sensor can be implemented in the Wheatstone bridge using TMR devices with different topologies, and the merit is that the output voltage of the bridge can be adapted to be independent of the change in the ohmic resistance (thermal-drift

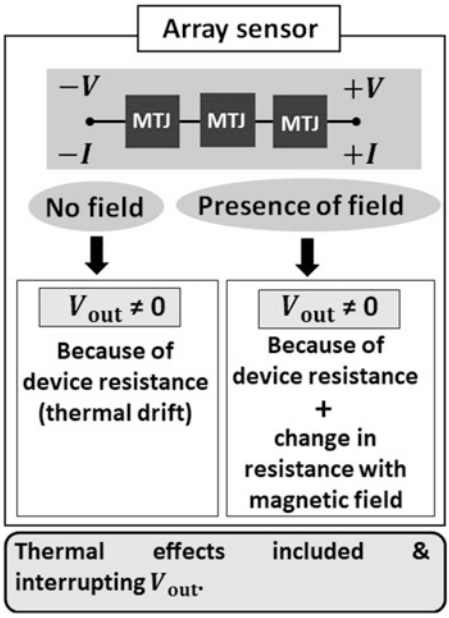

Fig. 11 Output signal of MTJ array sensor with and without external magnetic field; thermal-drift current contributing the output voltage/resistance change in the two cases. (Adapted with permission from Ref. [48], Copyright 2022, MDPI)

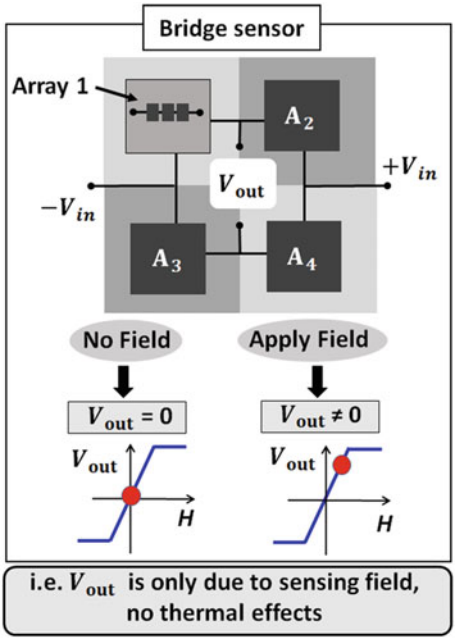

Fig. 12 Output signal of MTJ bridge sensor with and without external magnetic field; thermal-drift current not affecting the output voltage/resistance change in the two cases. (Adapted with permission from Ref. [49], Copyright 2018, MDPI)

current) of those devices. To carry out such a configuration, the bridge may contain four congruent TMR sensors (A_1, A_2, A_3, and A_4) as shown in Fig. 14, and each two opposing elements must have a symmetric dR/dH. It means that each two TMRs (A_1 and A_4) exhibits $dR/dH > 0$ and the other two (A_2 and A_3) exhibit $dR/dH < 0$. Then, unlike an individual TMR sensor or array, if R of each TMR array changes, the contribution of such a change to the output voltage (V_{out}) has nonsense.

The most-straightforward approach to implement a bridge TMR sensor is to connect all four TMR elements mechanically, either through wire bonding or at the PCB level, and align the matching elements in the similar direction but in the reverse sense. However, this technique has three significant drawbacks:

1. Alignment mistakes will always be introduced during mechanical assembly of the individual components; in turn, it will limit the performance of the device.
2. The mass production is not cost-effective for the mechanical assembly of individual components.
3. In compact applications demanding strong spatial regularity, mechanical rotation cannot be functioned because the separate parts will be relatively small to manipulate. A procedure to create entire Wheatstone bridges at the wafer level is necessary when such restrictions are present.

Sensor Evaluation Parameters

Sensitivity, electronic noise level, and limits of detection are three critical parameters that must be considered for any type of sensor, because those parameters involve a deterministic role in the sensors' application areas. Magnetic anisotropy has a vital impact on sensor sensitivity and limits of detection. Generally, uniaxial and unidirectional magnetic anisotropies are preferable because they provide a coherent rotation of magnetization and a reversible mechanism of magnetization, therefor a repeatable voltage response [50, 51]. Here the uniaxial magnetic anisotropy can stem from shape of a material (shape anisotropy) [52] and/or material's structure (magnetocrystalline anisotropy) [50], while the unidirectional anisotropy can be induced either by exchange bias (in FM/AFM bilayers and in FM/NM/AFM trilayers) or Ruderman–-Kittel–Kasuya–Yosida (RKKY) interaction between two ferromagnetic materials (separated by a nonmagnetic material: FM/NM/FM) [51]. The type and magnitude of a magnetic anisotropy can influence a sensor's sensitivity and limits of detection, particularly for materials that have uniaxial and unidirectional magnetic anisotropies.

Sensitivity

The sensor's sensitivity is stated as the occurring resistance derivative (as an output) divided by the magnetic field (as an input). Consequently, presuming the response in a linear way, the sensitivity attributed to MTJ sensors (S) is determined by the linear span's slope, which might be normalized by least resistance value (R_{min}) of the sensor to contrast the sensitivity of diverse sensors [53, 54]:

$$S = \frac{(R_{\max} - R_{\min})}{(R_{\min})} \frac{1}{\Delta H} = \frac{TMR}{\Delta H} \tag{8}$$

where $R_{\max}$ is the maximum sensor resistance value and ΔH represents the linear operating range. Thus, an elevated sensitivity is realized by limiting the field of saturation and raising the ratio for TMR. Though, the TMR ratio relies on the applied voltage magnitude, being roughly constant when the biasing voltage is reduced than 30 mV, until it begins to reduce nearly linearly approaching a magnitude which signifies 50% of the optimum TMR ratio (TMR_0). $V_{(1/2)}$ is the designation for the corresponding voltage magnitude where the signal reduces to half of its optimal value. Accordingly, the relation governing the dependence of TMR and biasing voltage values is introduced as follows:

$$[\mathrm{TMR(V)}] = \left[\mathrm{TMR}_0\left(1 - \frac{V}{2V_{\frac{1}{2}}}\right)\right] \tag{9}$$

Defects in the insulating barrier, which initiate to appear as the voltage elevates, are the main reason for the TMR reduction. Thus, an elevated-quality barrier is essential to diminish TMR−voltage reliance and advance junction specifications. An insulating barrier as a dielectric which might be disturbed electrically when the bias voltage exceeds the breakdown voltage ($V_{\mathrm{break}} \approx 1.5$ V) is introduced. This restriction can be overcome by employing a sensor array since it increases the entire voltage by dropping the voltage throughout every junction.

The magnitude of the applied voltage impacts the TMR amount; likewise, the sensor sensitivity owes a dependence on the biasing voltage amount represented mathematically as follows [55]:

$$[S(V)] = \left[S_0\left(1 - \frac{V}{2V_{\frac{1}{2}}}\right)\right] \tag{10}$$

where S_0 is the supreme sensitivity, acquired at reduced bias voltages. Within the linear section of the output curve, the resistance of the sensor can be labeled as a summation of a nominal resistance R_0 and an adjustable resistance ΔR_{H} which is affected by the magnetic field application H and the sensitivity of the sensor [55]:

$$R(H) = R_0 + \Delta R_{\mathrm{H}} = R_0 + S(V) R_{\min} H \tag{11}$$

where R_0 is the sensor resistance in the absence of the magnetic field, which might be designated as an offset term. Accordingly, the signal discrepancy ΔV because of an external magnetic field alteration $\Delta V = H_2 - H_1$ is assumed by

$$\Delta V = (R(H_2) - R(H_2))I \approx S(V)\, R_{\min} I \Delta H \tag{12}$$

Noise

Frequency-independent white noise (i.e., thermal noise and shot noise) and noise that is frequency-reliant on ($1/f$ flicker noise and random telegraphic noise [RTN]) are two forms of noise that are present in magnetic sensors. Also, the measurement circuit comprising amplification and electronics parts contributes with background noise, which influences the intrinsic signal of the sensors.

White Noise

Nyquist noise or thermal noise is the first typical sort of white noise. Any resistance at a temperature more than zero is a potential cause of electrical noise. When the electromotive force is absent, the electron velocity tends to be zero. However, Brownian motion delivers nonzero resistance fluctuations.

At a specific temperature T, the voltage spectral density specified with the thermal noise $S_{V,th}^{1/2}$ is given by the Nyquist formula (15), where k_B is Boltzmann constant, T is the temperature, and R is the magnetic sensor resistance. Nyquist noise (also known as thermal noise) is the first type of white noise. Electrical noise can come from any resistance at any temperature other than zero. In the absence of electromotive force, electrons have no velocity. However, Brownian motion causes resistance fluctuations to be nonzero. The Nyquist formula (13) gives the voltage spectral density of thermal noise S (V,th) at a constant temperature T: [55]

$$S_{V,th}^{1/2} = \sqrt{4k_B TR} \tag{13}$$

As clearly seen from Eq. 15, thermal noise does not depend on the applied voltage or magnetization characteristic of the device, but on the resistance (R). Compared to longitudinal resistances in AMR, GMR, and TMR devices, the transverse resistance in PHE-based sensors is very small. Therefore, thermal noise is very low in PHE-based magnetic field sensors.

Shot Noise

Shot noise is the second variety of white noise. It is an electrical noise that the Poisson law can simulate. Shot noise is a distinct carrier charge reflection. An electric current is produced by each charge carrier being transported when exposed to an electric field. Dissimilar to thermal noise, this noise is directly correlated with the electric current I and the carrier's charges. The following equation can be used to get the spectral noise density [36, 55]:

$$S_{V,\text{shot}}^{1/2} = \sqrt{2eIR} \tag{14}$$

Herein, e represents the electron charge, I is the applied current, and R is the resistance under study. This term is very low in AMR- and GMR-based sensors and virtually missed in PHE-based sensors. However, shot noise becomes important in

TMR-based sensors since the insulating layer causes a discontinuity in a conduction medium.

Flicker Noise

Flicker ($1/f$) noise is present in any type of material, and it is very rich in information about the quality of materials and layer structures. Particularly in low frequency applications of MR-based sensors, it is the major contributor to electronic noise. It can stem from the fluctuations of energy around equilibrium and is determined through the shape, size, and materials specifications For example, in magnetic materials, the presence of magnetic domains may cause a fluctuation of magnetization around the equilibrium energy (due to thermal activation, or stress, or vibrations). Flicker noise can be described by a general formula [36]:

$$S_{V,\frac{1}{f}}(f) = \frac{\alpha_H}{N} \cdot \frac{V^2}{f} \tag{15}$$

The terms in this Eq. N and V are designated as the overall charge carriers number and the potential difference within the conductor, respectively. The value of the nondimensional α_H known as the Hooge constant is varied with defect density and material purity, making it feasible to compare the noise levels of various sensors. Below the overlap (cutoff) frequency, the $1/f$ noise is responsible for the white noise (characteristically in GMR and TMR). For the small GMR magnetic sensor, the generated noise as a result of the magnetic domains is elevated and is closely correlated with the structural characteristics and magnetic configuration of the GMR. Increased sensor volume lowers the $1/f$ noise since it owes an inverse proportion to the number of carriers.

Random Telegraphic Noise

One of the most dynamic and significant source of variation in digital circuits is the random telegraph noise (RTN). The RTN arises as a result of random variation among magnetic domains of metastable states of the free layers. The RTN phenomenon inducing undesirable fluctuations in the electrical resistance is largely related to the working circumstances of the used device and also on the induced polarization current. The spectral density of RTN is given in Eq. 16:

$$S_{V,RTN}(f) = S_{V,RTN}(0) / \cosh\left(\frac{\Delta E}{k_B T}\right) \left[\cosh^2\left(\frac{\Delta E}{k_B T}\right) + (2\pi f \tau)^2\right] \tag{16}$$

where $\tau^{-1} = \sum_{i=1}^{2} {\tau_i}^{-1}$ with $\tau_i = \tau_{i,0} \exp\left(\frac{E_i}{K_B T}\right)$ and E_i corresponds to the energy level residing at state i. In magnetoressitive sensors, appearance of RTN is mainly due to magnetic fluctuations associated with magnetic instability of the magnetic layers and particularly fluctuations during the magnetization reversal process at the pinning sites.

Detectivity

The threshold magnitude, which designates the lowest external magnetic field that the sensor can detect at a specific frequency with a specified bandwidth, is used to express the sensor's detectability. Thus, a signal beyonds the threshold range will not produce an output alternation because of the limit of detection and the sensor noise. The sensor detectivity is expressed in magnetic field units corresponding to the noise level as in the following equation [36, 56]:

$$D = \frac{S_{\mathrm{V}}^{\mathrm{total}}}{S\, I_{\mathrm{bias}}\, R_0}\ (\mathrm{Oe/Hz}) \tag{17}$$

$S_{\mathrm{V}}^{\mathrm{total}}$ is the entire magnitude of noise and S is the sensitivity for the sensor, being together determined at a specified bias voltage through an external magnetic field H.

Magnetic Sensor Applications

Recently, the fast development of the micro- and nanotechnology related areas impacts an immense portion of the scientific development delivering an elevated life quality experience [57]. A variety of sensing systems demonstrate an extensive assortment of thoughts and phenomena from the of physics and material science fields [3]. The rapid acquisition of the test results, reduced cost fabrication and processing, and feasibility of usage are significant requirements for the biological systems diagnostics [21]. The following section covers briefly the most common industrial and medical applications for magnetic sensors. Figure 13 represents major magnetic sensing applications.

Magnetocardiography (MCG)

Inaccessible health monitoring has developed a need because of limited healthcare access arising from lockdowns for pandemic and elevated aging populations [59]. Medical applications relying on magnetic sensing appliances might be divided into two major categories: the measurements of exerted fields delivered by the organs in humans and the monitoring of the magnetically labeled beads and macromolecules. The potential evolution of the magnetic field sensors directed toward medical applications demands a specific focus on the noise reduction and enhancing the entire device to be smaller, affordable, and cheaper while at the same time maintaining the desired amounts of the detection limit [21]. Figure 14 presents versatile magnetic sensing selectivities. Here, magnetic cardiography as a medical application for magnetic sensors is introduced. Magnetocardiography refers to the

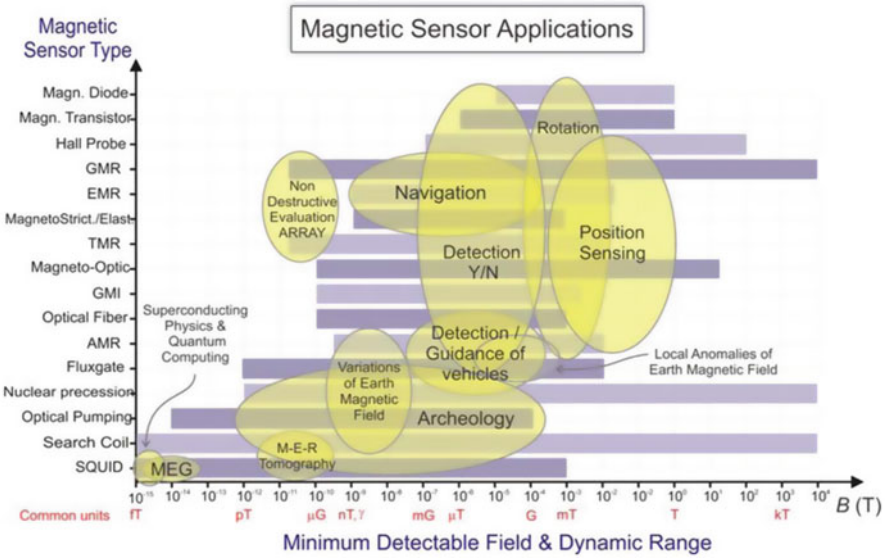

Fig. 13 Major magnetic sensing technologies and their linked application areas. (Reproduced with permission from Ref. [58], Copyright (2009), MDPI publisher)

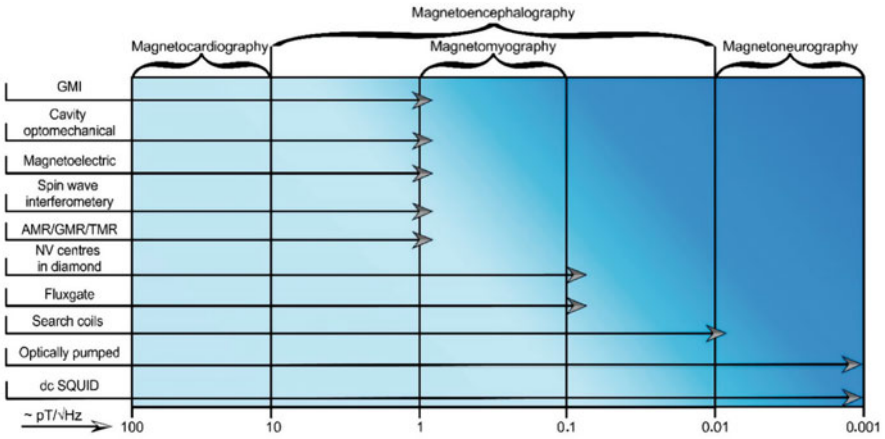

Fig. 14 Different magnetic sensors technologies reflected on the vertical axis with respect to the biomagnetic detection signals on the horizontal axis. (Adapted with permission from Ref. [21], Copyright 2020, MDPI)

technique which detects the appraising magnetic fields arising from the heart's electric currents and activities which cardiomyocytes generate. This process employs highly sensitive devices like the SQUID [60]. Magnetic cardiography provides early data for the conduction disturbances during the human fetal period.

Table 1 Advantages of MCG compared to ECG [60]

Parameter	MCG	ECG
The contribution of the basic currents	High	Low
Volume currents portion	Low	High
Effect of body tissues on conductivity	Low	High
Required attachment to the skin	No	Yes
The interference between the skin and electrode	No	Yes
Required filtering for straight current	No	Yes
The usage of fetal study	Yes	No

This might support in taking an early decision-making by physicians. Magnetocardiography (MCG) outcomes the electrocardiography (ECG) in terms of the performance and desired results due to their significant diagnostic potentials. Table 1 summarizes the completeness between MCG and ECG. Both ECG and MCG rely on the same phenomena; however, MCG are superior. This superiority emerges from the nature that MCG records direct magnetic fields from the primary current, while ECG results are recorded from the derived current from the primary one [60]. This nature delivers enhanced and less distorted information. Besides, conductivity is constant and independent of the body compositions in the case of MCG, while it fluctuates with dissimilar body compositions in ECG detected currents case [61]. The contactless, noninvasive MCG monitoring technique reduces skin electrode influence while simultaneously speeding up examinations. Last but not the least, the currents for MCG do not need any filtration; therefore, the MCG can assess the heart current absolute magnitude. The common benefits of the MCG over ECG are represented in Table 1. Versatile works have employed the magnetic cardiography for medical field, for instance, Sadman Sakib et al. have established a model that relied on artificial intelligence (AI) which merges two designs intending to simulate arrhythmia detection. The authors concluded that the designated AI architecture is auspicious for keeping the ultra-edge sensing appliances in the medical sector [59]. In another report, the authors have developed precise TMR sensors to evaluate both MCG and MEG at ambient conditions with a decent SNR and high spatial resolution [62]. The real on-time estimation and mapping of MCG affords a significant enhancement in heart disease diagnostic tools. The introduction of magnetocardiograms without the need for a magnetically shielded room has been recently developed by researchers [63]. In their work, they have delivered a setup which allows the clear detection of the magnetic field for the heart at ambient temperature in the absence of a shielded room. The authors have employed the TMR sensors to acquire low detection limits and precision by limiting the device and surrounding noise with a mathematical algorithm. In comparison with SQUID, it is more efficient due to less cost and time. These recent reports with a focus on the merging and combining of electronics, modeling, and basic physics could provide insights on grasping very promising selectivities and conditions for operation to assist in the detection of risks and potential dangers for human life.

Neural Signal Detection

The conducted massive research on the structure, behavior, and functions of our brain has been increased in the past few decades. These researches unable us to get more information and deep understanding of our brain; hence, a lot of funded programs are directed to this field.

Particular attention has been paid to healthcare and medical diagnosis fields; the analysis of brain signals can be helpful for identifying some diseases. Additionally, modern technology based on the brain–computer interface (BCI) that receives and processes real-time signals from our brain contributes to identifying some diseases and other different fields. For instance, neuroprosthetics can substitute a disabled person's nonfunctional arm or leg and be employed in neural repair and rehabilitation. The real-time signals of our brain could be used in many applications including video game interaction. The very complicated weak electrical signals generated from our brain in a very short period of time cause variation in the magnetic field of our brain.

Highly sensitive and accurate sensor arrays composed of superconducting quantum interferential devices (SQUIDs) were used for neural signal measuring and analyzing since early times, thanks to elevated ratio for accuracy and sensitivity. Nevertheless, the SQUIDs require a very low temperature to sustain the superconducting property during measurements; thereby, complicated and large scale devices are required.

From other point of view, the magnetic tunnel junction (MTJ) sensor based on the CMOS can be operated at room temperature and has a simple structure and low cost.

The alpha rhythm, one of the brain oscillations, has a frequency range of 8–13 Hz and reaches its maximum amplitude over the occipital area. Besides, it typically manifests in REM sleep, sleepiness, and peaceful wakefulness with the eyes closed, with an amplitude that diminishes when the eyes are opened. Based on this function, it can be used to monitor levels of wakefulness or identify drowsiness while driving. Additionally, the alpha rhythm can have a significant impact on other measurements of the brain activities like event-related field (ERF) due to its high amplitude. The ERF is a collection of brain activity that has been time-locked to an event, such as a sensory stimulus or the identification of a target stimulus, and is captured using magnetic tunnel junctions. It is the measurable brain activity that follows a particular sensory, cognitive, or motor event. In this regard, recording brain signals using linear MR sensors has been examined [64–67].

Nondestructive Detection (NDT)

Magnetic NDT technologies have been widely implemented in manufacturing to guarantee the functioning protection of ferromagnetic assemblies and apparatuses [68]. Ferromagnetic materials are composed of magnetic domains at the microstructural level. One characteristic property of these ferromagnetic materials is the existing coupling through the emerging stress and the magnetic field where the

magnetization might promote a distortion in the FM dimensions known as magnetostriction [68]. Conversely, applied stress and mechanical forces also alter the FM magnetization referred to as the piezomagnetic effect [68]. These phenomena are attributed to the rotation of magnetic moments and subsequent domain wall movement upon the experience of external magnetic fields or mechanical forces. The latter (i.e., piezomagnetic effect) has seized raised interest due to the suitability of evaluating stress status by magnetic measurement devices. Consequently, noteworthy efforts and techniques have been focused on this section in the preceding decades such as magnetic flux leakage (MFL) and Barkhausen noise. The concept of the MFL working principle is based on the leakage of the magnetic field whenever magnetic field is applied to ferromagnetic material. This leakage is pursued by the potential existence of any geometrical asymmetry. The arising leakage can be monitored by magnetic sensors to report the dimensions of the defect [69, 70]. The important parameters to consider for this leakage are as follows: 1) The flux should be large enough, systematic, and homogenous to enable the variation at the defect place. 2) The appropriate positioning of the sensor is necessary to differentiate between the arising leakage due to the defect and the background noise. Hoke first revealed the MFL phenomenon in 1918, and the initial application of the MFL technology was conducted by Watts in 1933 for evaluating welded joints [68]. The pipeline pig is considered as a successful application of MFL where it was functioned for the corrosion of metals in oil pipelines. Figure 15 represents this design. Despite the facility provided for the MFL as a nondestructive testing approach, two parameters need more investigation and optimization. The first is the changed dimensions of the defect (i.e., width, depth, length) and so forth which impact the measurement signals, and second is the burden of dealing with elastic-plastic regions close to the cracks. Therefore, more research is demanded on these points [68, 71]. The nondestructive analysis covers a wide range of areas including magnetic flux leakage, magnetic particle inspection, and recently the protection of cultural heritage. The nondestructive process is achievable with a neural network design introduced by Doulmais in 2012 [72]. This design has the capability for detecting the artistic styles involved in paintings. NDT can also be incorporated for delivering messages on the initial case of a building or a construction to aid in realizing the

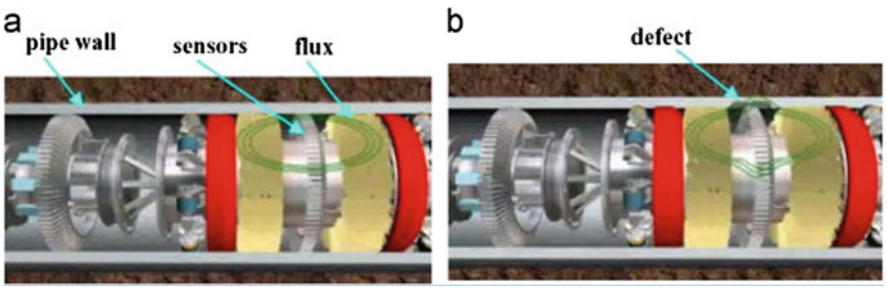

Fig. 15 The design of the called pipeline pig. (**a**) No defect is detected in the pipeline, and (**b**) the defected site is monitored. (Adapted with permission from Ref. [68], Copyright 2012, Elsevier)

errors beforehand. This way limits the loss of life [73]. Like so, this technique is beneficial for preserving cultural heritage and national treasures.

Monitoring of Pollutants in Water Resources

Water treatment for the groundwater and available water resources has been greatly demanded in the recent decades. This necessity is specifically vital in water-rich countries and communities [74]. The resulting contaminations from industrial factories, pesticides, and other sources might raise the potential of diseases and deliver undesired risks for human health and the environment including animals. Additionally, food industry might contain various sorts of pollutants such as water organic pollutants (e.g., cationic and anionic dyes). The progress of low-cost and label-free sensors is demanded to mitigate the influences of water limitation and contamination. Agriculture and other related fields' productivity is elevated as the sensors can regulate the environmental situations by reducing the inputs and allowing the employment of pesticides and water more affordably. Besides, these sensors are beneficial in digitizing irrigation concepts [75]. The most common sources for water pollutants are illustrated in Fig. 16. The detection and estimation of these contaminations assists in designing proactive solutions to provide higher quality water. The manipulation of these pollutions as an applied answer and sensing and gaging the capacities of these toxic materials can profit designing a practical consequence to eradicate the toxins and enhance the water value. Versatile approaches have been paved to determine the pollutants in water such as spectroscopic analysis [76],

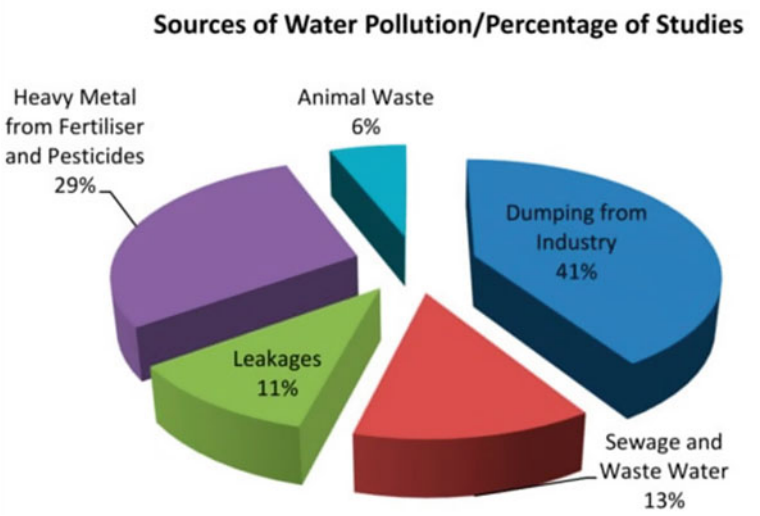

Fig. 16 Various surrounding sources for water contamination. (Adapted with permission from Ref. [80], Copyright 2021, MDPI)

chromatographic studies [77], or more [78]. For the application of determining heavy metals, pollutants, and contaminations, there might be few undesirable disadvantages like side toxicity, prolonged time process, reduced sensitivity, and costly methods. The electrochemical sensing approach is introduced for the removal of toxins and contaminations [9, 11, 79]. However, the benefits offered by magnetic sensing technologies using sensors and composites are superior and provide insights on the needed application, and it is remotely controlled by the external applied field. The common sources of water pollution are introduced in Fig. 16.

Magnetic materials include three subcategories which are ceramics, alloys, and composites. Among them, ferrite- and iron-based composites as magnetite and hematite are widely exploited for the pollutant removal from water resources in various sensing technological aspects [74]. Magnetic materials possess a few desirable merits such as the ability for functionalization, biocompatibility, separation, and cost [74]. The challenge is generally to control the synthesis process to acquire tailored morphology, size, and stability conditions. In this contest, 2D transition-metal carbide materials stated as nanocomposites are auspicious entrants with various striking features. They have widely spanned versatile sorts of applications including cancer therapy, imaging processes, and particularly water treatment. On the one side, MXenes tend to agglomerate as major magnetic materials behave and it can be oxidized. Besides, separation in aqueous media is harsh because of the high colloidal ability. The increased size of the MXene molecules hinders transfer of the electrons at the interface and suppresses the formation of a suitable contact surface for electron transfer. Being said, the MXene based magnetic materials act as an environmental remedy for the removal of toxins and heavy metals. Though, the functionalization of the surface is beneficial and requested for the upsurge of efficiency and disadvantages elimination, as well as to avoid wasted time and cost. Thus, the functionalization of the surface has evolved to afford metal oxide nanocomposites for the eradication of pollutants and contaminations [81]. The hybridization of $Fe_2O_3/Ti_3C_2T_x$ which is a magnetic MXene nanocomposite was synthesized using the hydrothermal process to purify the mercury (Hg^{2+}) ions accompanied by other metal ions (Na^+, K^+, Ca^{2+}) from the medium. Inherently, the metal ions were reduced by this composite as an adsorber, and the mercury concentration approached 0.02 mg^{-1} after starting at 2.29 mg^{-1}. This removal proficiency might be attributed to the presence of extra anion groups such as O^{2-} and OH^- which are negatively charged on the surface [82]. Reported in another research, Shahzad et al. synthesized nanosheets of MXene to eradicate copper from water. The results indicate that MXene has the ability for removal according to excellent surface area and hydrophilicity. That mechanism was evaluated by the contributing functional groups of O, OH, and F on the MXene surface as potential locations to absorb the heavy metal ions [83]. Many other combinations based on MXene and other nanocomposites [84] have functioned for the remediation of water. In summary, several desirable specifications and merits as the hydrophobic attitude, less toxicity, and raised area of the surface nominate the MXene and their combined nanocomposites for water treatment. Generally, there are three sorts of applications, for membranes, electrodes, and adsorbents. To keep the flow of the work and the

progress of the magnetic materials-based sensing routes, the hazardous pollutants in water resources might be eradicated by other routes besides the already published ones, suggesting the combination of magnetic materials with other nonmagnetic matrices to limit the agglomeration incident and upsurge the efficiency of application. The other possible direction is to hit the manipulation and control of waterborne pathogens and bacteria. The evolution of potential materials for detecting waterborne viruses and bacteria in various aqueous environments could elevate the evaluation quality as these bacteria and viruses are generally resisting the antimicrobial agents. Besides, it is also necessary to fabricate innovative designs that could simultaneously assess various sorts of contaminants in water resources efficiently and precisely to save time, cost, and effort. Finally, machine learning and artificial intelligence are impacting everything in our progressively propagating life activities; therefore, the simulation models using these machine learning and artificial intelligence methods for the hazardous are also demanded. Few reports are inspected in this regard [85]. The employment of smart wearable tools for the prediction and monitoring of these pollutants is highly suggested.

Conclusion

The magnetic sensors are widely spread in various types and sorts, based on the orientation of the field and magnetization along with the magnetic moments. The classification as AMR, GMR, TMR, PHE or other is grasped. The parameters optimizing the performance of the sensor are mainly the sensitivity, the detection limit or the resolution, the exchange-bias field, as well as the magnetic anisotropy and noise. Depending on the specific area of application, these parameters can be manipulated and optimized. Magnetic sensor applications have the advantage of being tracked and employed in a wireless method. Therefore, they are applied on a wide scale of everyday life activities such as computer heads, microbead detection, MRI, automobile industry, magnetic cardiography, and more. Magnetic sensors are beneficial and need further investigation in the upcoming years along with the modeling and simulation devices supported with artificial intelligence and machine learning for the progress in the upcoming era.

Future Perspective

According to the sensor development roadmap published in 2019 [86], a research milestone is the development of stand-alone TMR sensors with magnetic field detectivity ≈ 1 pT/√Hz at 10 Hz by 2027. For ultraprecise applications such as detection of neural signals, magnetocardiography, and quantum computing systems, subpT magnetic field detectivity is also mandatory. For that, extensive research efforts have been done to achieve such a detection limit. Old-style research applies additional techniques as magnetic flux concentrator (MFC) to improve sensor sensitivity and hence improve detectivity. However, this technique is incompatible

with continuous minimization of electronic devices. Recently, great efforts have been made to optimize the shape, size, and aspect ratio of tunneling junctions. Also, the number of integrated junctions as an array or bridge sensor has also been investigated. However, there are still imitating parameters as the device footprint and background noise. Therefore, these techniques are considered as artificial ways to improve the limit of detection and are not treating the fundamental origin of the noise in multilayer spintronic stacks. Therefore, very recent attention has been paid to optimize the soft-magnetic properties and the crystal structure of magnetic materials especially in the free layers. For instance, utilizing amorphous phase of CoFeBTa, with high crystallization temperature $\geq 500\ ^{\circ}C$, helps to improve the bcc texture and minimize source of crystal defects at MgO/CoFeB interface as discussed in section "Sensor Materials." This improves the signal-to-noise ratio and thereby improves the detection limit. However, polycrystalline magnetic materials such as NiFe have better soft-magnetic properties than amorphous magnets. Therefore, materials engineering, integrating the properties of amorphous and polycrystalline magnetic materials, and introducing newly functional free layers are the future approaches to push the limit of detection towards subpico Tesla range. These types of magnetic sensors might provide a supportive apparatus for the upcoming era and the next generations.

References

1. Wilson JSBT-STH (2005) Chapter 1 – sensor fundamentals. Newnes, Burlington, pp 1–20
2. Rout CS, Hegde M, Govindaraj A, Rao CNR (2007) Ammonia sensors based on metal oxide nanostructures. Nanotechnology 18:205504. https://doi.org/10.1088/0957-4484/18/20/205504
3. Lenz J, Edelstein S (2006) Magnetic sensors and their applications. IEEE Sensors J 6:631–649. https://doi.org/10.1109/JSEN.2006.874493
4. Morsy M, Abdel-Salam AI, Mostafa M, Elzwawy A (2022) Promoting the humidity sensing capabilities of titania nanorods/rGO nanocomposite via de-bundling and maximizing porosity and surface area through lyophilization. Micro Nano Eng 17:100163. https://doi.org/10.1016/j.mne.2022.100163
5. Morsy M, Elzwawy A, Abdel-Salam AI, Mokhtar MM, El Basaty AB (2022) The humidity sensing characteristics of PANI-titania nanotube-rGO ternary nanocomposite. Diam Relat Mater 126:109040. https://doi.org/10.1016/j.diamond.2022.109040
6. Morsy M, Ibrahim M, Yuan Z, Meng F (2020) Graphene foam decorated with ZnO as a humidity sensor. IEEE Sensors J 20:1721–1729. https://doi.org/10.1109/JSEN.2019.2948983
7. Morsy M, Elzwawy A, Oraby M (2022) Carbon nano based materials and their composites for gas sensing applications. Egypt J Chem 65:1–2
8. Elzwawy A, Mansour AM, Magar HS, Hammad ABA, Hassan RYA, El Nahrawy AM (2022) Exploring the structural and electrochemical sensing of wide bandgap calcium phosphate/ $CuxFe_3$-xO_4 core-shell nanoceramics for H_2O_2 detection. Mater Today Commun 33:104574. https://doi.org/10.1016/j.mtcomm.2022.104574
9. El Nahrawy AM, Abou Hammad AB, Elzwawy A, Alam MM, Asiri AM, Uddin J, Kabir MH, Rahman MM (2022) Development of 4-aminophenol sensor probe based on co(0.8-x) $ZrxNa_{0.2}Fe_2O_4$ nanocomposites for monitoring environmental toxins. Emergent Mater 5:431–443. https://doi.org/10.1007/s42247-021-00342-y
10. El Nahrawy AM, Elzwawy A, Alam MM, Hemdan BA, Asiri AM, Karim MR, Hammad ABA, Rahman MM (2021) Synthesis, structural analysis, electrochemical and antimicrobial activities

of copper magnesium zirconosilicate ($Cu_{20}Mg_{10}Si_{40}Zr(30\text{-}x)O$:(x = 0,5,7,10) Ni^{2+}) nanocrystals. Microchem J 163:105881. https://doi.org/10.1016/j.microc.2020.105881
11. Abou Hammad AB, Elzwawy A, Mansour AM, Alam MM, Asiri AM, Karim MR, Rahman MM, El Nahrawy AM (2020) Detection of 3,4-diaminotoluene based on $Sr_{0.3}Pb_{0.7}TiO_3$/$CoFe_2O_4$ core/shell nanocomposite: via an electrochemical approach. New J Chem 44: 7941–7953. https://doi.org/10.1039/d0nj01074j
12. Mishra RB, El-Atab N, Hussain AM, Hussain MM (2021) Recent Progress on flexible capacitive pressure sensors: from design and materials to applications. Adv Mater Technol 6: 2001023. https://doi.org/10.1002/admt.202001023
13. Masihi S, Panahi M, Maddipatla D, Hanson AJ, Bose AK, Hajian S, Palaniappan V, Narakathu BB, Bazuin BJ, Atashbar MZ (2021) Highly sensitive porous PDMS-based capacitive pressure sensors fabricated on fabric platform for wearable applications. ACS Sens 6:938–949. https://doi.org/10.1021/acssensors.0c02122
14. Morsy M, Darwish AG, Mokhtar MM, Elbashar Y, Elzwawy A (2022) Preparation, investigation, and temperature sensing application of rGO/SnO_2/Co_3O_4 composite. J Mater Sci Mater Electron. https://doi.org/10.1007/s10854-022-09247-w
15. Chen H, Zhang L, Hu Y, Zhou C, Lan W, Fu H, She Y (2021) Nanomaterials as optical sensors for application in rapid detection of food contaminants, quality and authenticity. Sensors Actuators B Chem 329:129135. https://doi.org/10.1016/j.snb.2020.129135
16. Fang L, Jia M, Zhao H, Kang L, Shi L, Zhou L, Kong W (2021) Molecularly imprinted polymer-based optical sensors for pesticides in foods: recent advances and future trends. Trends Food Sci Technol 116:387–404. https://doi.org/10.1016/j.tifs.2021.07.039
17. Philip A, Kumar AR (2022) The performance enhancement of surface plasmon resonance optical sensors using nanomaterials: a review. Coord Chem Rev 458:214424. https://doi.org/10.1016/j.ccr.2022.214424
18. Qin J, Jiang S, Wang Z, Cheng X, Li B, Shi Y, Tsai DP, Liu AQ, Huang W, Zhu W (2022) Metasurface micro/nano-optical sensors: principles and applications. ACS Nano 16: 11598–11618. https://doi.org/10.1021/acsnano.2c03310
19. Heidari H, Nabaei V (2019) Magnetic sensors for biomedical applications. Wiley-IEEE Press, Hoboken
20. Coey JMD (2010) Magnetism and magnetic materials. Cambridge University Press, Cambridge
21. Murzin D, Mapps DJ, Levada K, Belyaev V, Omelyanchik A, Panina L, Rodionova V (2020) Ultrasensitive magnetic field sensors for biomedical applications. Sensors (Switzerland) 20: 1569. https://doi.org/10.3390/s20061569
22. Elzwawy A, Piskin H, Akdoğan N, Volmer M, Reiss G, Marnitz L, Moskaltsova A, Gurel O, Schmalhorst J (2021) Current trends in planar Hall effect sensors: evolution, optimization, and applications. J Phys D Appl Phys. https://doi.org/10.1088/1361-6463/abfbfb
23. Volmer M, Neamtu J (2012) Optimisation of spin-valve planar Hall effect sensors for low field measurements. IEEE Trans Magn 48:1577–1580. https://doi.org/10.1109/TMAG.2011.2173671
24. Lin G, Makarov D, Schmidt OG (2017) Magnetic sensing platform technologies for biomedical applications. Lab Chip 17:1884–1912. https://doi.org/10.1039/C7LC00026J
25. Damsgaard CD, Freitas SC, Freitas PP, Hansen MF (2008) Exchange-biased planar Hall effect sensor optimized for biosensor applications. J Appl Phys 103:07A302. https://doi.org/10.1063/1.2830008
26. Mahfoud M, Tran QH, Wane S, Ngo DT, Belarbi EH, Boukra A, Kim M, Elzwawy A, Kim C, Reiss G, Dieny B, Bousseksou A, Terki F (2019) Reduced thermal dependence of the sensitivity of a planar Hall sensor. Appl Phys Lett 115:072402. https://doi.org/10.1063/1.5110671
27. Elzwawy A, Kim S, Talantsev A, Kim C (2019) Equisensitive adjustment of planar Hall effect sensor's operating field range by material and thickness variation of active layers. J Phys D Appl Phys 52:285001. https://doi.org/10.1088/1361-6463/ab18f2
28. Talantsev A, Elzwawy A, Kim C (2018) Effect of NiFeCr seed and capping layers on exchange bias and planar Hall voltage response of NiFe/Au/IrMn trilayer structures. J Appl Phys 123: 173902. https://doi.org/10.1063/1.5023888

29. Freitas PP, Ferreira R, Cardoso S (2016) Spintronic sensors. Proc IEEE 104:1894–1918. https://doi.org/10.1109/JPROC.2016.2578303
30. Binasch G, Grünberg P, Saurenbach F, Zinn W (1989) Enhanced magnetoresistance in layered magnetic structures with antiferromagnetic interlayer exchange. Phys Rev B 39:4828–4830. https://doi.org/10.1103/PhysRevB.39.4828
31. Baibich MN, Broto JM, Fert A, Van Dau FN, Petroff F, Etienne P, Creuzet G, Friederich A, Chazelas J (1988) Giant magnetoresistance of (001)Fe/(001)Cr magnetic superlattices. Phys Rev Lett 61:2472–2475. https://doi.org/10.1103/PhysRevLett.61.2472
32. Rifai D, Abdalla AN, Ali K, Razali R (2016) Giant magnetoresistance sensors: a review on structures and non-destructive Eddy current testing applications. Sensors 16:298
33. Giouroudi I, Keplinger F (2013) Microfluidic biosensing systems using magnetic nanoparticles. Int J Mol Sci 14:18535–18556
34. Tripathy D, Adeyeye AO (2008) Current-perpendicular-to-plane giant magnetoresistance in half-metallic pseudo-spin-valve structures. J Appl Phys 103:07D702. https://doi.org/10.1063/1.2828617
35. Hirohata A, Yamada K, Nakatani Y, Prejbeanu L, Diény B, Pirro P, Hillebrands B (2020) Review on spintronics: principles and device applications. J Magn Magn Mater 509:166711. https://doi.org/10.1016/j.jmmm.2020.166711
36. Freitas PP, Ferreira R, Cardoso S, Cardoso F (2007) Magnetoresistive sensors. J Phys Condens Matter 19:165221. https://doi.org/10.1088/0953-8984/19/16/165221
37. Wang M, Zhang Y, Zhao X, Zhao W (2015) Tunnel junction with perpendicular magnetic anisotropy: status and challenges. Micromachines *6*(8):1023–1045
38. Lee D-Y, Lee S-E, Shim T-H, Park J-G (2016) Tunneling-magnetoresistance ratio comparison of MgO-based perpendicular-magnetic-tunneling-junction spin valve between top and bottom $Co_2Fe_6B_2$ free layer structure. Nanoscale Res Lett 11:433. https://doi.org/10.1186/s11671-016-1637-9
39. Matos F, Macedo R, Freitas PP, Cardoso S (2023) CoFeBX layers for MgO-based magnetic tunnel junction sensors with improved magnetoresistance and noise performance. AIP Adv 13:25108. https://doi.org/10.1063/9.0000559
40. Rasly M, Nakatani T, Li J, Sepehri-Amin H, Sukegawa H, Sakuraba Y (2021) Magnetic, magnetoresistive and low-frequency noise properties of tunnel magnetoresistance sensor devices with amorphous CoFeBTa soft magnetic layers. J Phys D Appl Phys 54:95002. https://doi.org/10.1088/1361-6463/abc2f5
41. Cardoso S, Leitao DC, Gameiro L, Cardoso F, Ferreira R, Paz E, Freitas PP (2014) Magnetic tunnel junction sensors with pTesla sensitivity. Microsyst Technol 20:793–802. https://doi.org/10.1007/s00542-013-2035-1
42. Wiśniowski P, Almeida JM, Cardoso S, Barradas NP, Freitas PP (2008) Effect of free layer thickness and shape anisotropy on the transfer curves of MgO magnetic tunnel junctions. J Appl Phys 103:07A910. https://doi.org/10.1063/1.2838626
43. Almeida JM, Freitas PP (2009) Field detection in MgO magnetic tunnel junctions with superparamagnetic free layer and magnetic flux concentrators. J Appl Phys 105:07E722. https://doi.org/10.1063/1.3077228
44. Leitao DC, Silva AV, Ferreira R, Paz E, Deepack FL, Cardoso S, Freitas PP (2014) Linear nanometric tunnel junction sensors with exchange pinned sensing layer. J Appl Phys 115:17E526. https://doi.org/10.1063/1.4869163
45. Oogane M, Fujiwara K, Kanno A, Nakano T, Wagatsuma H, Arimoto T, Mizukami S, Kumagai S, Matsuzaki H, Nakasato N, Ando Y (2021) Sub-pT magnetic field detection by tunnel magneto-resistive sensors. Appl Phys Express 14(12):123002. https://doi.org/10.35848/1882-0786/ac3809
46. Lu Y, Altman RA, Marley A, Rishton SA, Trouilloud PL, Xiao G, Gallagher WJ, Parkin SSP (1997) Shape-anisotropy-controlled magnetoresistive response in magnetic tunnel junctions. Appl Phys Lett 70:2610–2612. https://doi.org/10.1063/1.118933
47. Endoh T, Honjo H (2018) A recent progress of spintronics devices for integrated circuit applications. J Low Power Electron Appl 8(4):44

48. Zhao W, Tao X, Ye C, Tao Y (2022) Tunnel magnetoresistance sensor with AC modulation and impedance compensation for ultra-weak magnetic field measurement. Sensors 22:1021
49. Yan S, Cao Z, Guo Z, Zheng Z, Cao A, Qi Y, Leng Q, Zhao W (2018) Design and fabrication of full wheatstone-bridge-based angular GMR sensors. Sensors 18:1832
50. Schuhl A, Van Dau FN, Childress JR (1995) Low-field magnetic sensors based on the planar Hall effect. Appl Phys Lett 66:2751–2753. https://doi.org/10.1063/1.113697
51. Hung TQ, Oh S, Sinha B, Jeong J-R, Kim D-Y, Kim C (2010) High field-sensitivity planar Hall sensor based on NiFe/Cu/IrMn trilayer structure. J Appl Phys 107:09E715. https://doi.org/10.1063/1.3337739
52. Das PT, Nhalil H, Schultz M, Amrusi S, Grosz A, Klein L (2021) Detection of low-frequency magnetic fields down to sub-pT resolution with planar-Hall effect sensors. IEEE Sens Lett 5:1–4. https://doi.org/10.1109/LSENS.2020.3046632
53. Kim KW, Torati SR, Reddy V, Yoon SS (2014) Planar Hall resistance sensor for monitoring current. J Magn 19:151–154. https://doi.org/10.4283/JMAG.2014.19.2.151
54. Donolato M, Dalslet BT, Damsgaard CD, Gunnarsson K, Jacobsen CS, Svedlindh P, Hansen MF (2011) Size-dependent effects in exchange-biased planar Hall effect sensor crosses. J Appl Phys 109:064511. https://doi.org/10.1063/1.3561364
55. Ripka P, Arafat MMBT-RM in MS and ME (2019) Magnetic sensors: principles and applications. Elsevier, Oxford
56. Hung TQ, Oh S, Jeong JR, Kim CG (2010) Spin-valve planar Hall sensor for single bead detection. Sensors Actuators A Phys 157:42–46. https://doi.org/10.1016/j.sna.2009.11.033
57. Vitol EA, Novosad V, Rozhkova EA (2012) Microfabricated magnetic structures for future medicine: from sensors to cell actuators. Nanomedicine 7:1611–1624. https://doi.org/10.2217/nnm.12.133
58. Díaz-Michelena M (2009) Small magnetic sensors for space applications. Sensors 9:2271–2288
59. Sakib S, Fouda MM, Al-Mahdawi M, Mohsen A, Oogane M, Ando Y, Fadlullah ZM (2022) Deep learning models for magnetic Cardiography edge sensors implementing noise processing and diagnostics. IEEE Access 10:2656–2668. https://doi.org/10.1109/ACCESS.2021.3138976
60. Watanabe S, Yamada S (2008) Magnetocardiography in early detection of electromagnetic abnormality in ischemic heart disease. J Arrhythmia 24:4–17. https://doi.org/10.1016/S1880-4276(08)80002-6
61. Nousiainen J, Oja S, Malmivuo J (1994) Normal vector magnetocardiogram: II. Effect of constitutional variables. J Electrocardiol 27:233–241. https://doi.org/10.1016/S0022-0736(94)80007-3
62. Fujiwara K, Oogane M, Kanno A, Imada M, Jono J, Terauchi T, Okuno T, Aritomi Y, Morikawa M, Tsuchida M, Nakasato N, Ando Y (2018) Magnetocardiography and magnetoencephalography measurements at room temperature using tunnel magneto-resistance sensors. Appl Phys Express 11:23001. https://doi.org/10.7567/APEX.11.023001
63. Kurashima K, Kataoka M, Nakano T, Fujiwara K, Kato S, Nakamura T, Yuzawa M, Masuda M, Ichimura K, Okatake S, Moriyasu Y, Sugiyama K, Oogane M, Ando Y, Kumagai S, Matsuzaki H, Mochizuki H (2023) Development of magnetocardiograph without magnetically shielded room using high-detectivity TMR sensors. Sensors 23:646
64. Amaral J, Cardoso S, Freitas PP, Sebastião AM (2011) Toward a system to measure action potential on mice brain slices with local magnetoresistive probes. J Appl Phys 109:07B308. https://doi.org/10.1063/1.3562915
65. Amaral J, Gaspar J, Pinto V, Costa T, Sousa N, Cardoso S, Freitas P (2013) Measuring brain activity with magnetoresistive sensors integrated in micromachined probe needles. Appl Phys A Mater Sci Process 111:407–412. https://doi.org/10.1007/s00339-013-7621-7
66. Caruso L, Wunderle T, Lewis CM, Valadeiro J, Trauchessec V, Trejo Rosillo J, Amaral JP, Ni J, Jendritza P, Fermon C, Cardoso S, Freitas PP, Fries P, Pannetier-Lecoeur M (2017) In vivo magnetic recording of neuronal activity. Neuron 95:1283–1291.e4. https://doi.org/10.1016/j.neuron.2017.08.012
67. Sharma PP, Gervasoni G, Albisetti E, D'Ercoli F, Monticelli M, Moretti D, Forte N, Rocchi A, Ferrari G, Baldelli P, Sampietro M, Benfenati F, Bertacco R, Petti D (2017) Towards a

magnetoresistive platform for neural signal recording. AIP Adv 7:56706. https://doi.org/10.1063/1.4973947
68. Wang ZD, Gu Y, Wang YS (2012) A review of three magnetic NDT technologies. J Magn Magn Mater 324(4):382–388. https://doi.org/10.1016/j.jmmm.2011.08.048
69. Pham HQ, Le VS, Vu MH, Doan DT, Tran QH (2019) Design of a lightweight magnetizer to enable a portable circumferential magnetic flux leakage detection system. Rev Sci Instrum 90: 74705. https://doi.org/10.1063/1.5090938
70. Pham HQ, Tran BV, Doan DT, Le VS, Pham QN, Kim K, Kim C, Terki F, Tran QH (2018) Highly sensitive planar Hall magnetoresistive sensor for magnetic flux leakage pipeline inspection. IEEE Trans Magn 54:1–5. https://doi.org/10.1109/TMAG.2018.2816075
71. Gupta M, Khan MA, Butola R, Singari RM (2022) Advances in applications of non-destructive testing (NDT): a review. Adv Mater Process Technol 8:2286–2307. https://doi.org/10.1080/2374068X.2021.1909332
72. Aggelis DG, Soulioti DV, Barkoula NM, Paipetis AS, Matikas TE (2012) Influence of fiber chemical coating on the acoustic emission behavior of steel fiber reinforced concrete. Cem Concr Compos 34:62–67. https://doi.org/10.1016/j.cemconcomp.2011.07.003
73. Clausen JS, Nikolaos Z, Knudsen A (2012) Onsite measurements of concrete structures using impact-echo and impulse response. Emerg Technol Non-Destr Test V:117–122
74. Hojjati-Najafabadi A, Mansoorianfar M, Liang T, Shahin K, Karimi-Maleh H (2022) A review on magnetic sensors for monitoring of hazardous pollutants in water resources. Sci Total Environ 824:153844. https://doi.org/10.1016/j.scitotenv.2022.153844
75. Mahmoud AED, Fawzy M (2021) Nanosensors and nanobiosensors for monitoring the environmental pollutants BT. In: Makhlouf ASH, Ali GAM (eds) Waste recycling technologies for nanomaterials manufacturing. Springer International Publishing, Cham, pp 229–246
76. Jung B, Safan A, Batchelor B, Abdel-Wahab A (2016) Spectroscopic study of se(IV) removal from water by reductive precipitation using sulfide. Chemosphere 163:351–358. https://doi.org/10.1016/j.chemosphere.2016.08.024
77. Allpike BP, Heitz A, Joll CA, Kagi RI, Abbt-Braun G, Frimmel FH, Brinkmann T, Her N, Amy G (2005) Size exclusion chromatography to characterize DOC removal in drinking water treatment. Environ Sci Technol 39:2334–2342
78. Holkar CR, Jadhav AJ, Pinjari DV, Mahamuni NM, Pandit AB (2016) A critical review on textile wastewater treatments: possible approaches. J Environ Manag 182:351–366. https://doi.org/10.1016/j.jenvman.2016.07.090
79. Alam MK, Rahman MM, Elzwawy A, Torati SR, Islam MS, Todo M, Asiri AM, Kim D, Kim CG (2017) Highly sensitive and selective detection of Bis-phenol A based on hydroxyapatite decorated reduced graphene oxide nanocomposites. Electrochim Acta 241:353–361. https://doi.org/10.1016/j.electacta.2017.04.135
80. Antwi HA, Zhou L, Xu X, Mustafa T (2021) Progressing towards environmental health targets in China: an integrative review of achievements in air and water pollution under the "ecological civilisation and the beautiful China" dream. Sustainability 13:3664
81. Hojjati-Najafabadi A, Mansoorianfar M, Liang T, Shahin K, Wen Y, Bahrami A, Karaman C, Zare N, Karimi-Maleh H, Vasseghian Y (2022) Magnetic-MXene-based nanocomposites for water and wastewater treatment: a review. J Water Process Eng 47:102696. https://doi.org/10.1016/j.jwpe.2022.102696
82. Shahzad A, Rasool K, Miran W, Nawaz M, Jang J, Mahmoud KA, Lee DS (2018) Mercuric ion capturing by recoverable titanium carbide magnetic nanocomposite. J Hazard Mater 344: 811–818. https://doi.org/10.1016/j.jhazmat.2017.11.026
83. Shahzad A, Rasool K, Miran W, Nawaz M, Jang J, Mahmoud KA, Lee DS (2017) Two-dimensional Ti_3C_2Tx MXene nanosheets for efficient copper removal from water. ACS Sustain Chem Eng 5:11481–11488. https://doi.org/10.1021/acssuschemeng.7b02695
84. Aylaz G, Kuhn J, Lau ECHT, Yeung C-C, Roy VAL, Duman M, Yiu HHP (2021) Recent developments on magnetic molecular imprinted polymers (MMIPs) for sensing, capturing, and

monitoring pharmaceutical and agricultural pollutants. J Chem Technol Biotechnol 96: 1151–1160. https://doi.org/10.1002/jctb.6681
85. Li X, Yang Y, Yang J, Fan Y, Qian X, Li H (2021) Rapid diagnosis of heavy metal pollution in lake sediments based on environmental magnetism and machine learning. J Hazard Mater 416: 126163. https://doi.org/10.1016/j.jhazmat.2021.126163
86. Zheng C, Zhu K, de Freitas SC, Chang J, Davies JE, Eames P, Freitas PP, Kazakova O, Kim C, Leung C, Liou S, Ognev A, Piramanayagam SN, Ripka P, Samardak A, Shin K, Tong S, Tung M, Wang SX, Xue S, Yin X, Pong PWT (2019) Magnetoresistive sensor development roadmap (non-recording applications). IEEE Trans Magn 55:1–30. https://doi.org/10.1109/TMAG.2019.2896036